ACOUSTIC TOMOGRAPHY IN THE STRAITS OF FLORIDA

by

David Brian Chester

B.S. Southampton College of Long Island University
(1986)

Submitted in partial fulfillment of the
requirements for the degree of

Master of Science

at the

MASSACHUSETTS INSTITUTE OF TECHNOLOGY

and the

WOODS HOLE OCEANOGRAPHIC INSTITUTION

September 1989

Signature of Author .....

Joint Program in Physical Oceanography
Massachusetts Institute of Technology
Woods Hole Oceanographic Institution
July 26, 1989

Certified by .....

Paola Malanotte-Rizzoli
Associate Professor of Physical Oceanography
Thesis Supervisor

Accepted by .....

Carl Wunsch
Chairman, Joint Committee for Physical Oceanography
Massachusetts Institute of Technology
Woods Hole Oceanographic Institution

ACOUSTIC TOMOGRAPHY IN THE STRAITS OF FLORIDA

by
David Brian Chester

Submitted in partial fulfillment of the requirements for the degree of
Master of Science at the Massachusetts Institute of Technology
and the Woods Hole Oceanographic Institution
July 27, 1989

Abstract

Variability of the Florida Current has been monitored via acoustic tomography. A reciprocal tomography experiment was conducted in the eastern half of the Florida Straits during mid October and November, 1983. A triangular array of transceivers, with leg separations of approximately 45 kilometers, was deployed at 27°N. The presence of a surface mixed layer in the region allowed for the ducted propagation of acoustic energy in the surface layer. A deeper layer was sampled by an unresolved group of refracted, bottom reflected ray arrivals. Incorporating the complete set of arrivals, we are able to obtain depth dependent estimates of the temperature field, current velocity, and relative vorticity. The oceanography of the region has been shown to be dominated by the lateral shifting of the surface and subsurface core of the Florida Current. The influx of westward flowing water through the Northwest Providence Channel at 26°N also appears as a large scale signal in the eastern Florida Straits. Low frequency fluctuations of temperature, current velocity, and vorticity occur at periods ranging from several days to nearly two weeks, and are intimately related to meandering of the Florida Current system.

Thesis Supervisor:
Dr. Paola Malanotte-Rizzoli, Associate Professor
Massachusetts Institute of Technology

Contents

Abstract **2**

Acknowledgments **5**

1 Introduction **6**

1.1 Historical Backgound 6

1.2 Thesis Overview 8

2 The Florida Straits Tomography Experiment **10**

2.1 Oceanography of the Region 10

2.2 Experimental Design 15

2.3 Environmental Data 19

2.4 The Processed Data 24

3 Ocean Acoustics and the Forward Problem **33**

3.1 Ray Theory 33

3.2 Ray Arrivals in Shallow Water 39

3.3 Formulation of the Forward Problem 54

4 The Inverse Problem **59**

4.1 Formulation of the Inverse Problem 59

4.2 The Singular Value Decomposition 63
4.3 Resolution and Variance 70

5 Oceanographic Variables **75**

5.1 Temperature 75
5.2 Current Velocity 80
5.3 Vorticity 84
5.4 Discussion and Conclusions 87

References **89**

Acknowledgments

First and foremost, I would like to thank my thesis advisor, Paola Malanotte-Rizzoli, for the continual guidance, enthusiasm, encouragement, and freedom she has given me along the way. The acoustic data set was graciously provided by Harry DeFerrari and his group at the University of Miami, RSMAS. The STACS current meter mooring data was provided by Rainer Zantopp, Friedrich Schott, and Tom Lee, also from the University of Miama, RSMAS. Numerous people have aided me in the development of this thesis, but I would especially like to thank Carl Wunsch, Jim Lynch, Harry DeFerrari, Dong-Shan Ko, and Bill Johns for stimulating discussions concerning various aspects of the thesis, and oceanography in general. Thanks also go to Anne-Marie Michael for assistance in the preparation of the manuscript.

This research was carried out under ONR contract N00014-86-K-0751.

Chapter 1

Introduction

1.1 Historical Backgound

The Florida Current plays a major role in the North Atlantic heat budget by transporting mass and warm water poleward through the Straits of Florida. The bathymetry of the Florida Straits, with Florida to the west and the Bahama Banks to the east, constrains the Florida Current to be a narrow, yet intense western boundary current. Upon exiting the Straits, the Florida Current evolves into a larger and more diffuse current as it connects with the Gulf Stream.

The study of the Florida Current is now over a century old. In a remarkable endeavor, Pillsbury (1891) directly measured currents to depths of 250 meters at various stations across the Straits and observed high frequency (tidal) oscillations of the flow, as well as lateral shifting of the Florida Current core. Volume transports of the Florida Current were calculated by Wüst (1924) and Parr (1937) using the dynamic height method. Montgomery (1938) and Hela (1952) noted seasonal fluctuations in the strength of the the Florida Current by observing sea level changes at tidal stations in the Straits. Large amplitude tidal and seasonal variations of the Florida Current mass transport were also obtained by Wertheim (1954) using the electropotential method with an underwater telegraph cable connecting Key West, Florida and Havana, Cuba.

Our understanding of the dynamics of the Florida Current has increased dramatically in the last twenty-five years as oceanographic instrumentation has evolved. Transport float measurements (Richardson and Schmitz, 1965; Schmitz, 1969; and Richardson et al., 1969) have given us a much clearer picture of the velocity structure of the Florida Current. Wunsch et al., (1969) used spectral analysis of tide gauge records to infer time scales of variability of the Florida Current. Nontidal fluctuations in the Florida Straits, with periods of several days to several weeks, have been related to atmospheric forcing by several authors (Düing et al., 1979; Wunsch and Wimbush, 1977; and Lee and Mayer, 1977). Mean kinetic and potential energy, as well as perturbation values, have been estimated across the Florida Straits (Brooks and Niiler, 1977). And most recently, the Subtropical Atlantic Climate Study (STACS) experiment was established to monitor long period fluctuations of mass and heat transport through the Florida Straits. Moored subsurface current meter arrays and the acoustic current profiler, along with tide gauges and a submarine cable, are the principal tools of measurement. Numerous papers concerning the spatial structure and temporal variability of the Florida Current have followed, including Molinari et al., 1985a,b; Lee et al., 1985; Leaman et al., 1987; Johns and Schott, 1987; and Schott et al., 1988.

Another technique for monitoring the activity of the Florida Current is acoustic tomography. Ocean acoustic tomography is a relatively new and promising method for determining oceanic structure and variability through the inversion of acoustic travel times to determine perturbations in sound speed (and hence temperature, density, and velocity). The idea was proposed by Munk and Wunsch (1979; 1982) as a practical tool for monitoring mesoscale fluctuations of an ocean basin. Several experiments have demonstrated the effectiveness of acoustic tomography in the mid ocean region (The Ocean Tomography Group, 1982; Cornuelle, 1983; Cornuelle et al., 1985; Howe et al., 1987). Until recently, it was not clear that tomography would be a viable approach in a shallow, range dependent region

such as the Florida Straits. Unlike the open ocean, where the SOFAR channel acts a natural waveguide in refracting acoustic rays towards its axis, the sound speed structure in the Straits is such that all rays are refracted downward and forced to bounce off the seabed. Palmer et al., (1985), using a specialized acoustic ray tracing program, found that the identification of individual ray paths in the Straits is nearly impossible due to uncertainties in bathymetry.

Ocean acoustic propagation in the Straits of Florida was first studied nearly twenty-five years ago during the MIMI experiments (Steinberg and Birdsall, 1966). The phase variations of a 420 Hz continuous wave signal transmitted across the Florida Current compared favorably with changes of transport and temperature (Steinberg et al., 1972). More recently, a tomography experiment was set up in the Florida Straits with the objective of determining the feasibility of measuring variability in the Straits via acoustic methods (DeFerrari and Nguyen, 1986). Two three-point reciprocal transmission experiments were conducted at 27°N in 1983. A small triangle, with leg separations of approximately 25 km, was situated on the western slope of the Straits. Results from this experiment can be found in DeFerrari and Nguyen, 1986; Ko, 1987; Monjo, 1987; and Ko et al., (1989). A larger triangular array, with leg separations of 45 km, was located on the eastern slope of the Florida Straits. This thesis will analyze the 40 day data set generated from the large triangle reciprocal tomography experiment of October, 1983.

1.2 Thesis Overview

The purpose of this thesis is to demonstrate the practicality of acoustic tomography as a monitoring scheme for a shallow water environment, specifically the Florida Straits. In so doing, it will be shown that accurate and reliable estimates of temperature, current velocity, and vorticity can be obtained quite readily. An

important result deriving from this thesis is the depth dependent estimation of the oceanographic variables.

The thesis is divided into five chapters. The 1983 Florida Straits tomography experiment is the subject of Chapter 2. To put the experiment in perspective, an overview of the hydrography of the Florida Straits region is given. A discussion of the experiment follows, along with the concurrent data from the STACS program. Finally, the processed acoustic data set is presented.

Chapter 3 introduces the forward problem of modelling acoustic propagation. Ray theory, based on Snell's law of refraction and the WKB approximation of a slowly varying medium with respect to acoustic wavelength, is chosen for the task. The principles of ray theory, and its application to a shallow water waveguide, are developed. The formulation of the forward problem then follows naturally.

The inverse problem is discussed in Chapter 4. The scheme of ocean acoustic tomography relies heavily on the machinery developed in the context of (geophysical) inverse theory. After formulating the inverse problem, a simple yet powerful solution technique is introduced, namely the singular value decomposition. The singular value decomposition provides an insightful link between the forward modelling and the acoustic data. A residual benefit of the decomposition is the estimation of model and data resolution and variance, and this topic will be considered in some detail.

Chapter 5 discusses the results obtained from the 1983 acoustic tomography experiment. Inversion estimates of temperature, along with estimates of current velocity and vorticity are presented, and comparisons are made with the more conventional oceanographic measurements. A thorough description of the time dependent oceanographic field is then given. Finally, the results obtained from the analysis are summarized.

Chapter 2

The Florida Straits Tomography Experiment

2.1 Oceanography of the Region

Before proceeding to a description of the oceanography of the Florida Current, the geographical setting is given. Figure 2.1 shows an overview of the region of study. The northern Straits of Florida (defined in this paper as extending from the tip of the Florida peninsula to the northern extent of the Little Bahama Bank) are the focus of this discussion. The coastline of Florida is the western boundary and the Bahama Banks are the eastern edge of the channel. The eastern boundary is not solid as the Northwest Providence Channel, reaching to a depth of 700 meters, divides the Great and Little Bahama Banks at latitude 26°N. A vertical slice through latitude 27°N is illustrated in Figure 2.2 to demonstrate the irregular bottom topography of the region. The seabed consists of a limestone (carbonate) base, with a surface layer of sediment a few meters thick (Malloy and Hurley, 1970).

The physical oceanography of the Straits of Florida is dominated by the Florida Current and its variability. The Florida Current is a northward flowing jet of warm water, with maximum surface velocities of 5 knots (2.5 m/s). The mass transport across the northern Straits is $30 \pm 5 \times 10^6$ m^3/s, with an associated heat flux of 1-2 $\times$ 10^{15} watts. Despite the lateral constraints of the Florida peninsula and the Bahama Banks, meandering of the Florida Current is a commonplace occurence.

Meandering events typically extend several tens of kilometers in the lateral direction and hundreds of kilometers in the along-stream direction. The temporal variability of the Florida Current is a complex amalgamation of time scales, with equally energetic perturbations occurring with tidal, weekly, and seasonal periodicities.

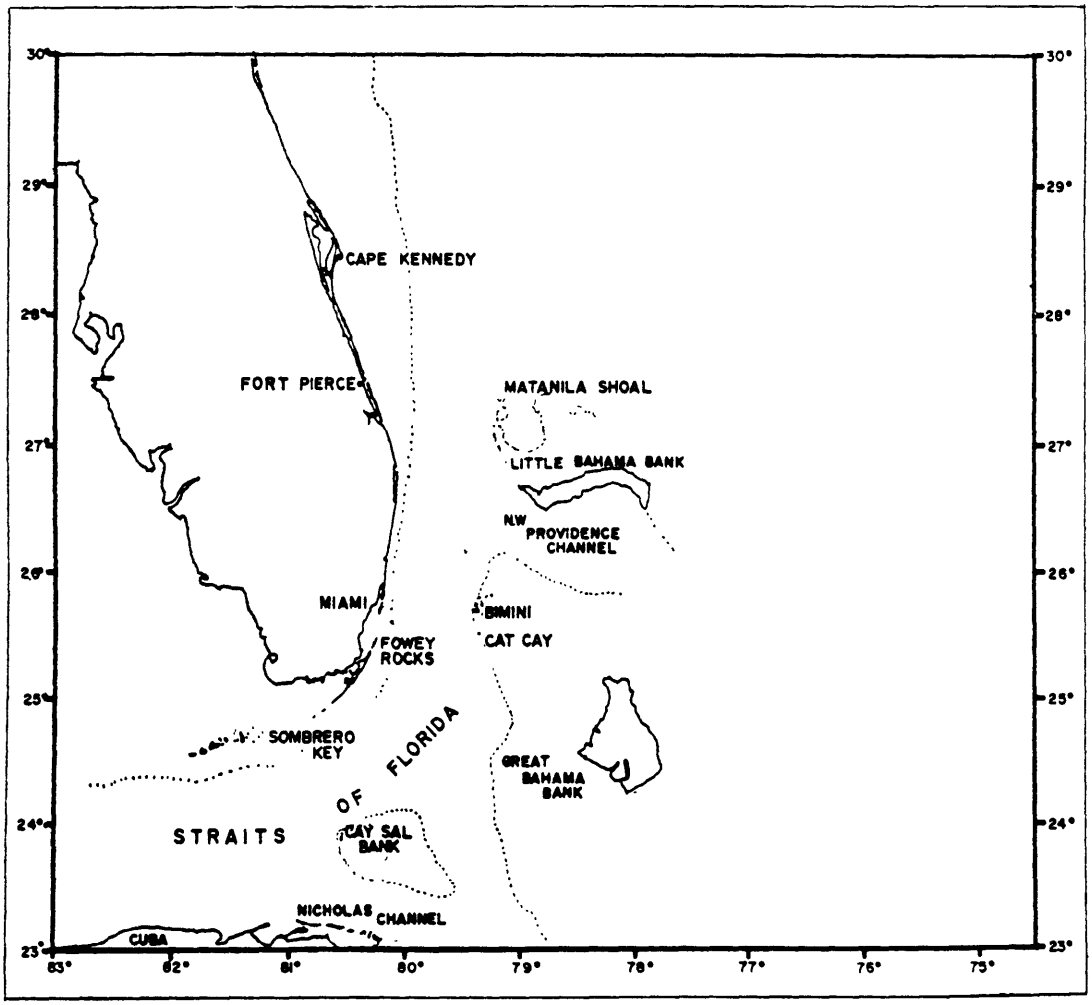

Figure 2.1. An overview of the Florida Straits region, (adapted from Richardson et al., 1969). The dotted line represents the 100 fathom contour.

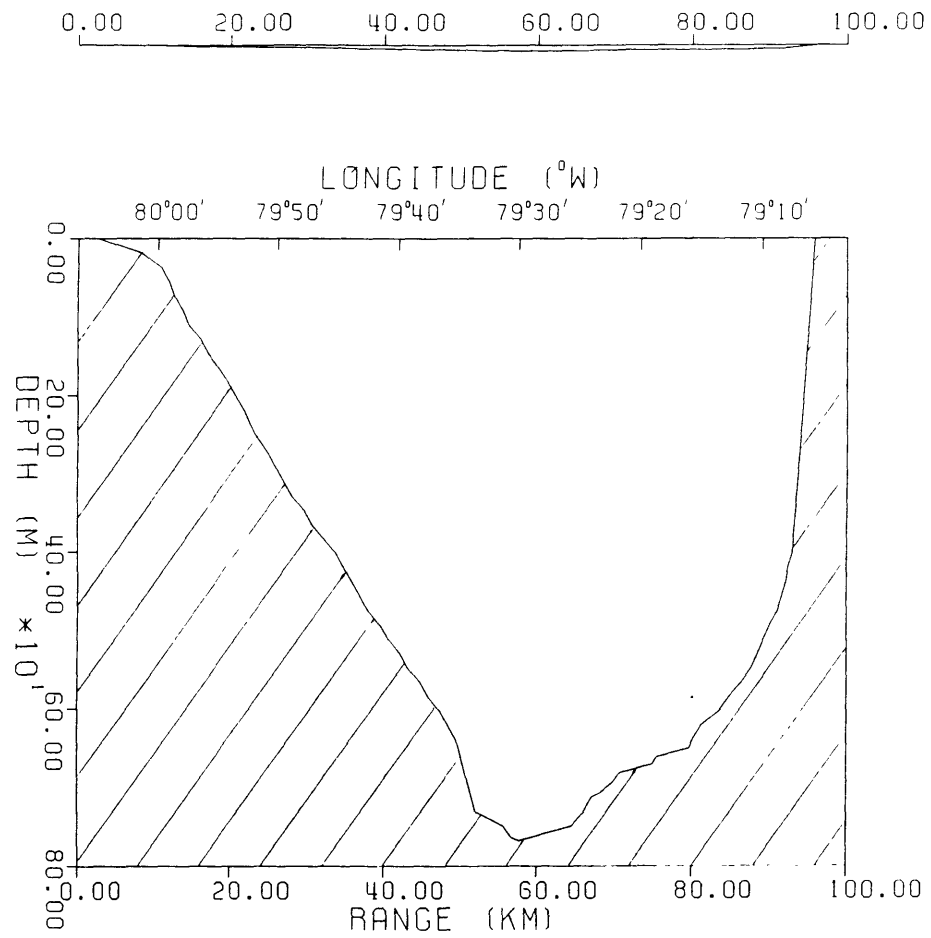

Figure 2.2. The bathymetry of the Florida Straits at 27°N. Vertical exaggeration is 1.0×10^2 in the lower graph. The upper graph shows a one to one scale of the bottom profile.

An 'average' picture of the Florida Current at latitude 27°N, as seen by the Pegasus acoustic current profiler, is illustrated in Figure 2.3 (from Leaman et al., 1987). Figures 2.3a-c show cross sections of average east and north current velocity components and temperature, respectively, and Figures 2.3d-f show the associated standard deviations. Several important features should be pointed out. The core of the maximum surface velocities is displaced toward the western continental slope of Florida. In addition, the core of the current gradually shifts offshore with depth.

A highly baroclinic structure is evident as the current speed decreases rapidly with depth. Looking at the horizontal shear (which is dominated by $\frac{dv}{dx}$ as $v >> u$), a strong cyclonic shear zone is seen on the onshore side of the current and an anticyclonic region exists on the offshore edge. Also noteworthy is a large scale westward flow encroaching from the Northwest Providence Channel. Finally, the downward sloping of the isotherms from west to east is consistent with a geostrophic northward flow.

As previously mentioned, fluctuations of current velocities and temperature in the 2 to 20 day frequency band is dominated by energy associated with Florida Current meanders. Johns and Schott (1987) find that the most coherent, energetic meandering events occur at periods near 5 and 12 days. The downstream propagation of the 5 day (12 day) meander is found to have a phase speed of 36 km/d (28 km/d) and a wavelength of 170 km (340 km). The passage of meanders leads to a 'sloshing' of the thermocline, with upwelling and downwelling of isopycnals rearranging the cross stream structure of the current (Johns, personal communication). Several mechanisms have been proposed for the generation of meanders in the Florida Current, such as shelf waves and barotropic and baroclinic instability in the presence of topography. The interaction of the Florida Current with the local topography of the Great Bahama Bank and Little Bahama Bank has been suggested as a source for larger scale variability in the Straits (Leaman and Molinari, 1987). Brooks (1975) proposes that a fluctuating wind stress can induce cross shelf perturbations via upwelling or downwelling associated with the Ekman transport being offshore or onshore. The jury is still out as to whether or not variations in local wind stress and wind stress curl are a primary source of energy for the meandering.

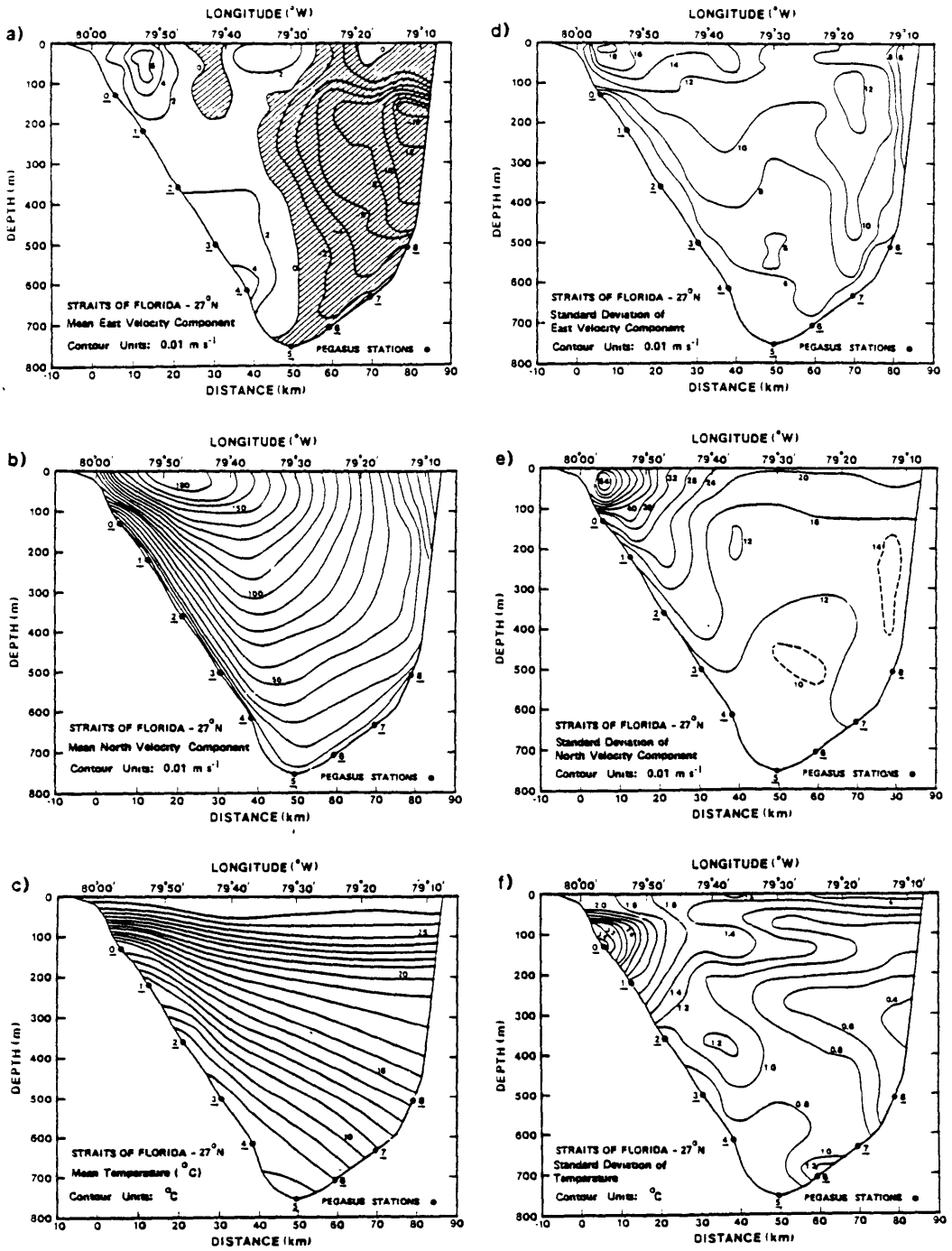

Figure 2.3. The ensemble average (a-c) and standard deviation (d-f) of east and north velocity components and temperature, respectively, based on results of 16 Pegasus cruises to the Florida Current at 27°N, (adapted from Leaman et al., 1987).

2.2 Experimental Design

The October 1983 acoustic tomography experiment consisted of a triangular array of transceivers (with units acting as both sources and receivers) situated at 27°N in the eastern half of the Florida Straits (see Figure 2.4). Transceivers 1 (26°56′N, 79°41′W) and 2 (27°19′N, 79°41′W) are aligned nearly longitudinally, with transceiver 3 (27°07′N, 79°16′W) located just to the west of Little Bahama Bank. All three instruments were moored at a depth of 38 meters above the bottom. The distances between units 1-2, 1-3, and 2-3 are 41.5 km, 46.5 km, and 46.4 km, respectively. Figure 2.5 shows the bathymetry along the three legs of the triangle. Note that the leg connecting transceivers 1 and 2 is aligned almost parallel with the axis of the Florida Current, and the corresponding bottom topography is relatively flat. On the other hand, transmission from units 1 and 2 to 3, and vice versa, occurs over a steep and irregular bottom on the anticyclonic side of the Straits.

The resolvability of individual acoustic multipaths is a necessity in ocean acoustic tomography, and specialized signals have been developed for this task. The present day standard signal consists of a coded sequence of digits which exhibits pulselike characteristics upon reception and cross replication. Design of the signal involves several important tradeoffs which warrant a brief discussion. A high signal to noise ratio requires a powerful source. Identification of pulse arrival times requires a narrow pulse, and therefore a transmitted signal with a large bandwidth. But the transmission of a high power wide-band pulse is highly constrained by the limited power supply (batteries). Due to this limitation, transmissions are not continuous, but rather occur at regular intervals during most tomographic experiments. The typical multipath arrival signal is not an evenly spaced sequence of nonoverlapping delta functions. Instead, oceanic inhomogeneieties (such as internal wave fluctua-

tions) lead to constructive and destructive interference of multipaths, and a blurred envelope of arrivals which varies with time results. To overcome this problem, periodic pulses are transmitted and coherently averaged at the receiver to boost the signal to noise ratio. The maximum number of pulse repetitions is limited by the ocean coherence time, which is generally considered to be several minutes. For more details of the signal design and processing for tomography, the reader is referred to excellent discussions given by Spindel (1985) and Metzger (1983).

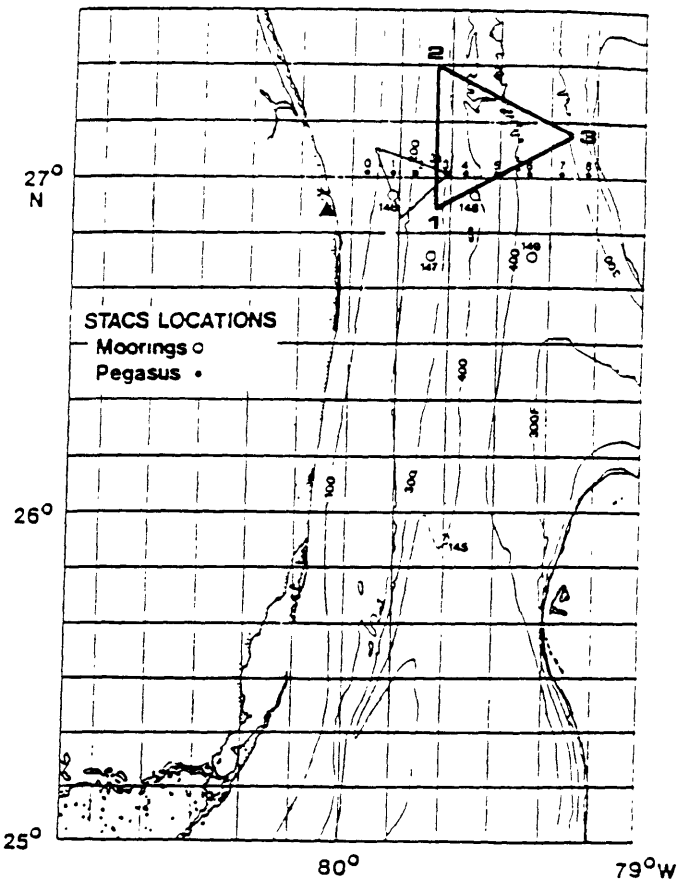

Figure 2.4. Location of the October 1983 tomography array (large triangle), (adapted from DeFerrari and Nguyen, 1986). Also shown is the location of the August 1983 tomography array (small triangle), along with STACS 4 moorings 146-149, and Pegasus stations 0-8.

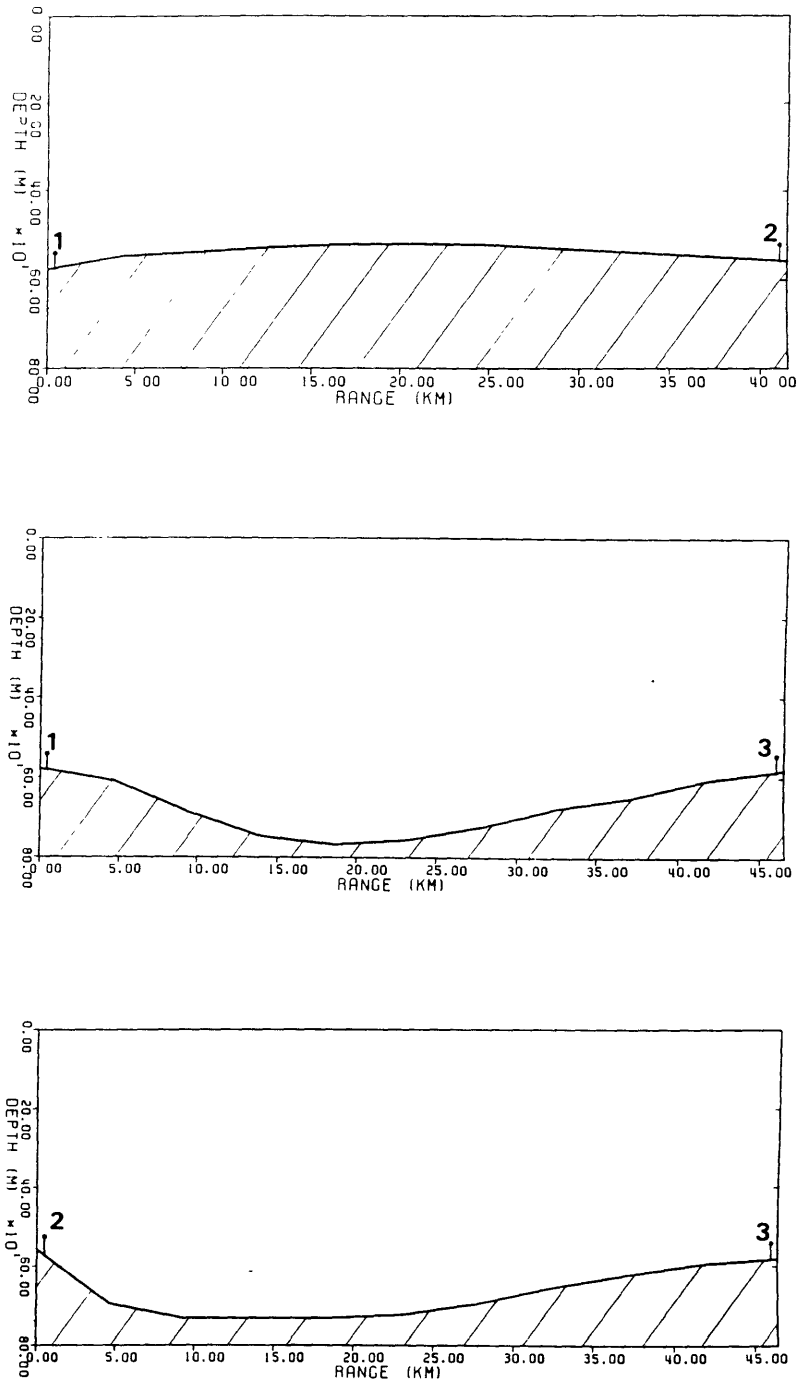

Figure 2.5. Bottom topography along the three legs of the tomographic array. The transceivers are moored 38 meters above the bottom.

Getting back to the 1983 tomography experiment, the transmitted signal consisted of a frequency modulated linear maximal pseudorandom sequence. The carrier frequency was 459.5588 Hz, with a bandwidth of 100 Hz. The source level was approximately 176 db re 1 μPa at 1m. The repetition period of the transmitted signal (2.2 s) was greater than the total spread of multipath arrivals (1.5 s), so no overlapping of arrivals occurred. A summary of the signal parameters for the 1983 large triangle experiment is given in Table 1.

Table 1: Signal Parameters for the October 1983 Florida Straits Experiment

Carrier frequency	459.5588 Hz
Bandwidth	100 Hz
Digits	255
Digit duration	0.0087 s
Sequence duration	2.2195 s
Repetitions	135 (4.99 min)

The transmission schedule commenced (time 0) with unit 1 transmitting (for approximately 5 minutes) to units 2 and 3, which received and processed the signal. Approximately 2 minutes after the first transmission (or 7 minutes from time 0), unit 2 transmits to units 1 and 3. The two minute wait is necessary to allow for propagation of the signal (which takes nearly 30 seconds) and processing of the received signal. Approximately 2 minutes later (or 14 minutes from time 0) unit 3 transmits to units 1 and 2. The entire 'sing around' time takes about 20 minutes. The instruments then wait until the beginning of the next hour (approximately 40 minute wait period) to repeat the cycle.

The received signals were first bandpass filtered, amplified, then sampled at four times the carrier frequency. The next step was complex demodulation (a pulse compressing summation process). The resulting demodulates were then coherently averaged with subsequent sequences (over the full 5 minute period), yielding a record of 510 complex demodulate pairs. The demodulate pairs were then stored internally on a cassette tape. Correlation with a replica of the transmitted linear maximal pseudorandom sequence was not done in situ.

The October 1983 acoustic tomography experiment generated a complete 40 day data set of reciprocal hourly transmissions for all three instruments.

2.3 Environmental Data

We are fortunate that the October 1983 tomography experiment occurred simultaneously with the STACS program. A subsurface moored array of Niskin Wing and Aandera current meters was maintained across the Florida Straits for several years (see Figure 2.4 for the location of the STACS 4 moorings). Direct measurements of current velocities and temperature at several depths were recorded. A sawtooth array was deployed in hopes of studying meandering variability and propagation. A vertical slice through 27°N is pictured in Figure 2.6, showing the spatial coverage of the STACS 4 array. Note that no current meters extend to the high velocity core (upper 150 meters) of the Florida Current. In addition to the current meter data, Pegasus acoustic profiles of temperature and horizontal velocity were obtained at regular intervals at eight station across the Straits (see Figure 2.4 and 2.6 for locations of the Pegasus stations). The Pegasus data set is valuable because it gives us measurements over the entire water column, including the surface layer which is not sampled by the current meter array.

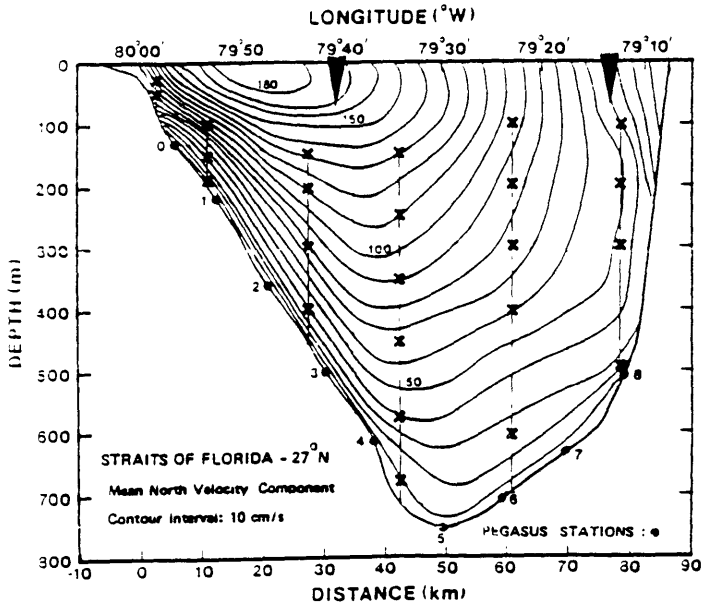

Figure 2.6. Moored current meter coverage superimposed on mean downstream velocity contours from Pegasus sections, (adapted from Leaman et al., 1987). The location of the Pegasus sections (0-8) are marked at the bottom. The triangles at the surface indicate the lateral extent of leg 1-2 and vertex 3 of the October 1983 tomography array.

Time series of velocity and temperature from the current meters are discussed first. Temperature time series (Figures 2.7a-c) and velocity time series (Figures 2.8a-c) are presented for moorings 147, 148, and 149 from the middle of October until the end of November. The temperature and velocity records have been 3 hour bandpass filtered, sampled at hourly intervals, then daily averaged. Mooring 147 is closely aligned with the 1-2 leg of our tomographic array, but displaced 20 km upstream. Time series from mooring 147 sample the eastern edge of the current core. Mooring 148 is located close to the lower leg of the tomographic array and captures much of the energetic variability of the current. Mooring 149 contains an incomplete record (with only one current meter yielding a full time series) of the eastern region.

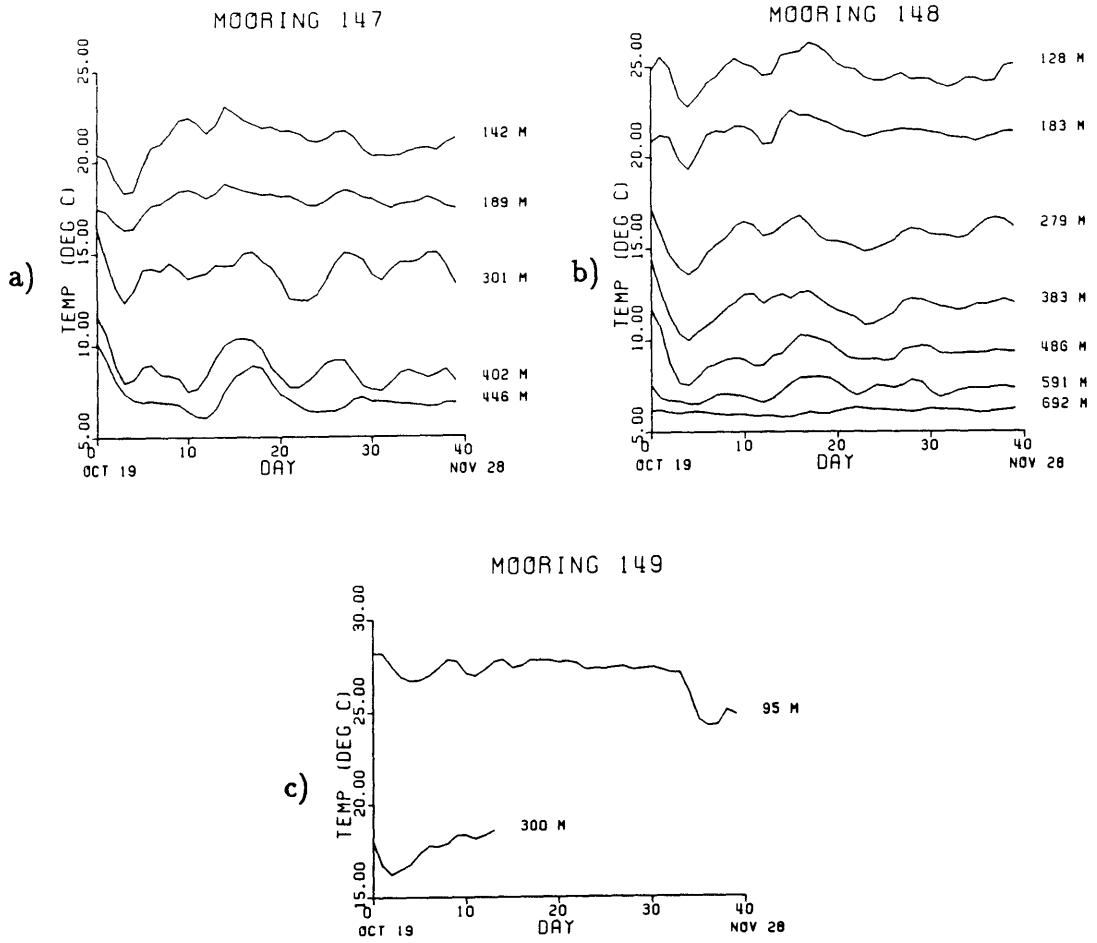

Figure 2.7. Time series of daily averaged temperature at each current meter for (a)mooring 147, (b)mooring 148, and (c)mooring 149. Day 0, the beginning of the experiment, corresponds to October 19.

We now turn to the Pegasus acoustic velocity profiler data set. A summary of Pegasus observations in the Florida Straits can be found in a report by Vertes and Leaman (1984). The Pegasus profiler is an acoustically tracked, free-falling instrument which gives continuous measurements of horizontal velocities and temperature (see Spain et al., (1983) for a complete discussion of the velocity profiler).

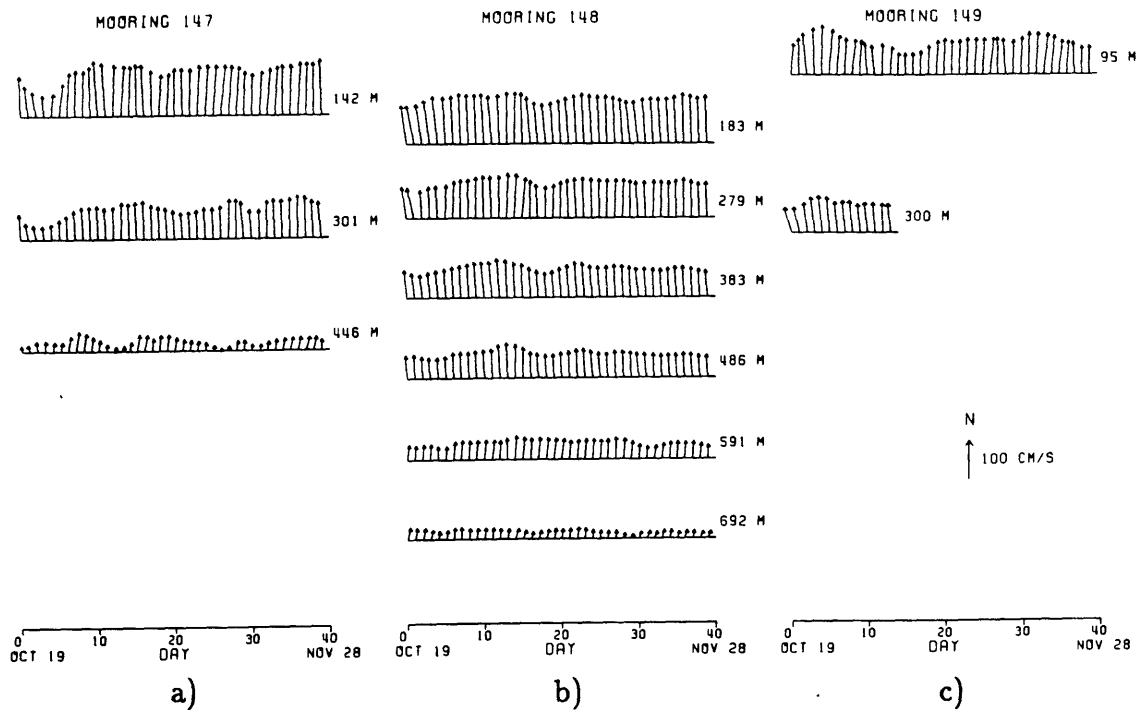

Figure 2.8. Time series (stick plots) of daily averaged current velocities at (a)mooring 147, (b)mooring 148, and (c)mooring 149. Day 0, the beginning of the experiment, corresponds to October 19.

Temperature profiles for stations 3a-7, averaged over five up/down casts and a several day period (October 28 - November 4) are presented in Figure 2.9. Note that station 3a is directly in line with the path connecting the north/south leg of the tomographic array.

A good picture of the oceanographic setting can be obtained from these two data sets. From the Pegasus data set, a nearly isothermal mixed layer extending to a depth of 100 meters is evident at all stations. Beneath the mixed layer the temperature decreases steadily with depth, with warmer water penetrating to greater depths as the Bahama Bank is approached. Typical current velocities at the top instruments ($\sim$ 150 m depth) are 100 cm/s. The highly baroclinic current is

quite coherent with depth. The mooring records show an energetic meandering event at the outset which is readily detected by the large drop in current velocity at mooring 147. Several smaller scale events, with periodicities near two weeks, are suggested by the temperature and velocity fluctuations. A detailed discussion of the oceanography will be presented in comparison with the inverse results in Chapter 5.

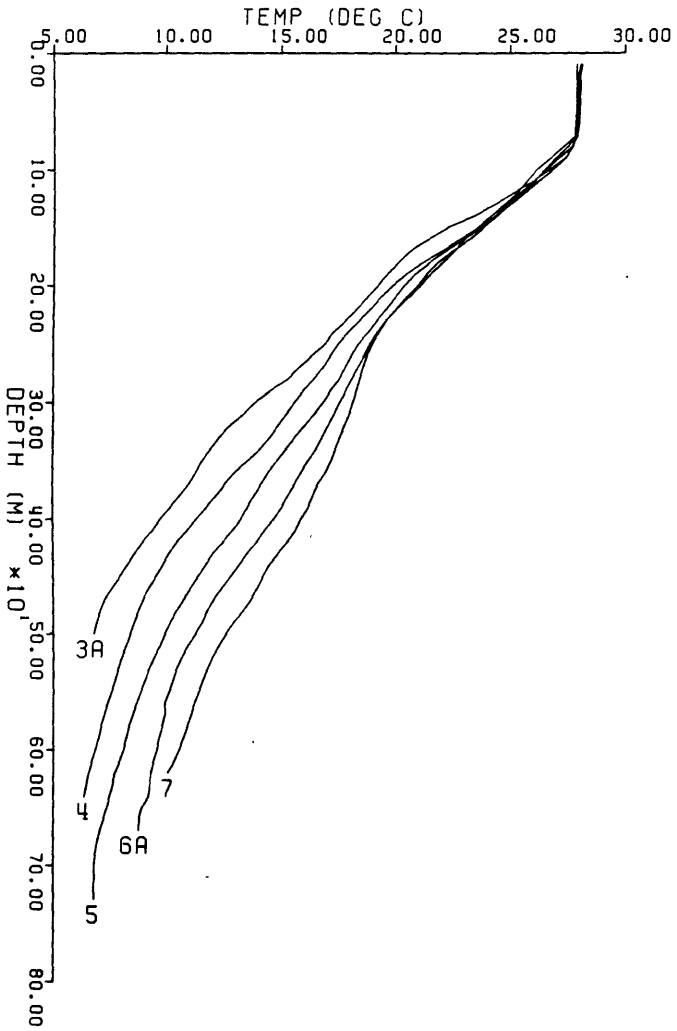

Figure 2.9. Average temperature profiles for late October - early November at Pegasus stations 3a-7.

2.4 The Processed Data

The received signal was first cross correlated with a replica of the transmitted signal. The result of this operation was a pulse response of 510 complex samples with a sampling interval of 4.352 ms (2.2195 s / 510 samples). This procedure was applied to all six records. Hereafter we will refer to the data records as S1R2 (signifying transmission from source 1 to receiver 2), S2R1, S1R3, S2R3, S3R1, and S3R2. The signal to noise ratio of an average pulse response was about 35 db (Table 2). It is not necessary to know the exact intensity of the pulse response as the inversion scheme used in this thesis is based on the travel time arrival of pulses.

Table 2: Signal to Noise Ratio

Source level	176 db re 1 μPa
Transmission loss	
Spherical spreading -20 $\log_{10}$R	-93 db
Attenuation loss .0168 db/km	-1 db
Received signal level (176-94)	82 db
Noise (1 Hz band)	-70 db
Bandwidth (100 Hz)	-20 db
Received signal to noise ratio (82-90)	-8 db
Processing gain	
Coherent averaging gain	
($10\log_{10}$(number of pulses - 2))	21 db
Pulse compression gain	
($10\log_{10}\frac{\text{sequence duration}}{\text{digit duration}}$)	24 db
Total signal processing gain	45 db
Signal to Noise Ratio of Typical Pulse (45 -8)	37 db

A typical pair of reciprocal hourly pulse responses of S1R2 and S2R1 is plotted in Figures 2.10a,b. Relative travel time is plotted along the abscissa, with time zero corresponding to the first of the 510 samples. Absolute travel time is not used for the acoustic record because of navigational inaccuracies in the determination of the source/receiver separation distance, and hence pulse arrival time. The ordinate represents signal to noise ratio, in db, for the first hourly pulse response. Consec-

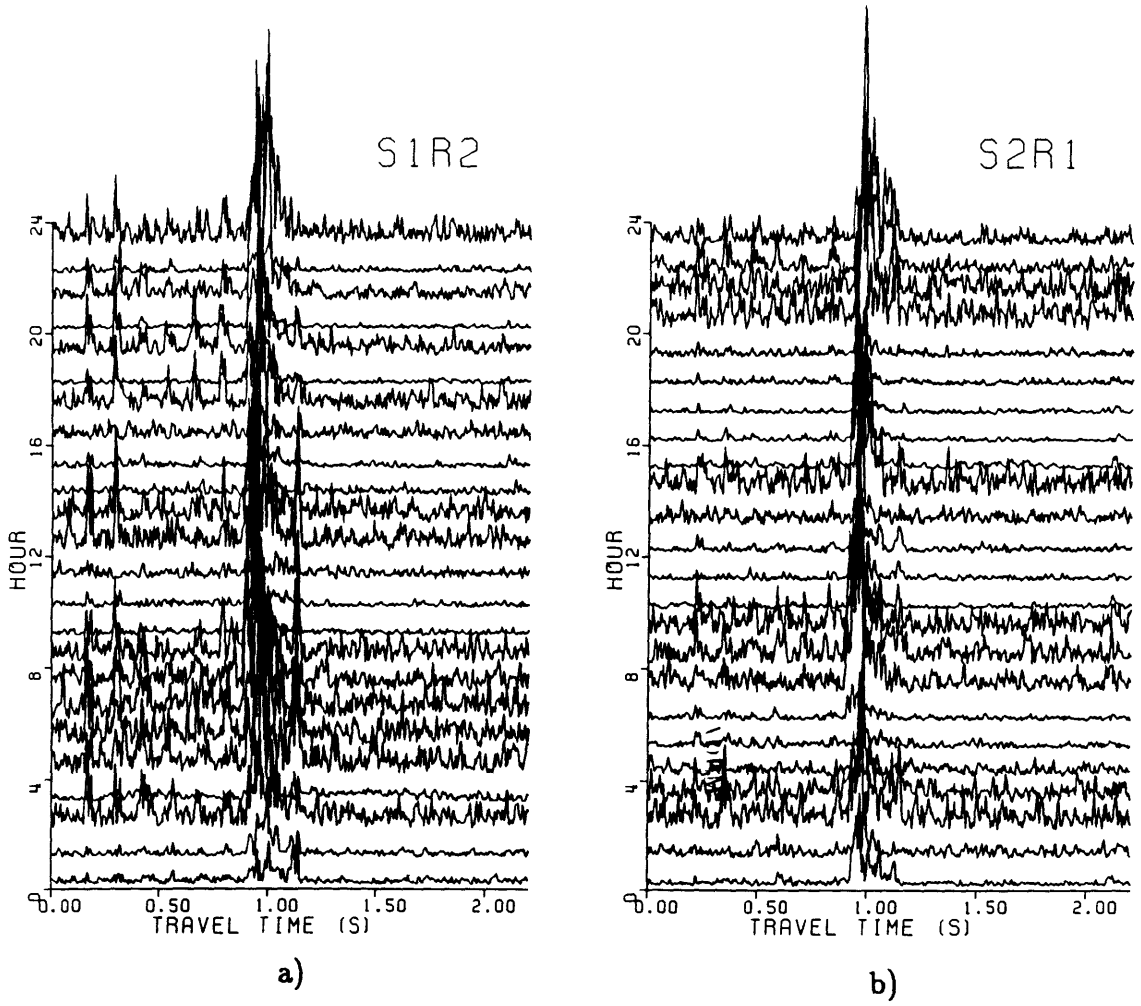

Figure 2.10. Reciprocal hourly pulse responses of (a)S1R2 and (b)S2R1 for a typical day (day 5 in this case). Relative travel time is plotted along the abscissa, with the ordinate representing the signal to noise ratio (or acoustic intensity).

utive hourly transmissions are then offset by a constant amount to aid in viewing. Looking closely at Figures 2.10a,b we see that identification of individual multipaths is not a simple task. The appearance and disappearance of multipaths is attributed to the influence of tides and internal waves. It is also evident that the hourly pulse responses from reciprocal transmissions are not identical.

A much clearer picture evolves when we take the daily average of 24 hourly pulse responses. By doing this we avoid aliasing of the dominant tidal and internal wave signals while simultaneously decreasing the random noise level. The six data records of daily averaged pulse responses, normalized by the daily averaged noise, are shown in Figures 2.11a-f. Several features are prominent in all of the plots. The most obvious signal is a large peak which is seen as the latest arrival in all records. This peak always exists, although the shape (multipath structure) varies from day to day. It will later be shown that this peak corresponds to a path of propagation which samples the lower 300 meters of the water column. The precursor arrivals, most evident in the pulse responses of S1R2 and S2R1, correspond to paths of propagation which are surface ducted. These early arrivals did not exist in the August 1983 experiment (Ko, 1987). Their appearance is due to the surface mixed layer which acts to trap rays. The pulse responses of daily averaged reciprocal transmissions are seen to be quite similar, with small scale differences still obvious. A further discussion of the pulse responses is given in Section 3.2 in conjunction with the ray theoretical arrival predictions.

Another issue to be discussed at this time is the identification of the processed pulse arrival times, and errors associated with this identification. Arrival times were estimated by taking the center of mass of the most intense peaks in the pulse response record. A minimum threshold was set, and only those peak samples which exceeded this limit were used in the estimate. The arrivals for S1R2 and S2R1 (except for day 10 where the noisy reception is not understood) are stable with

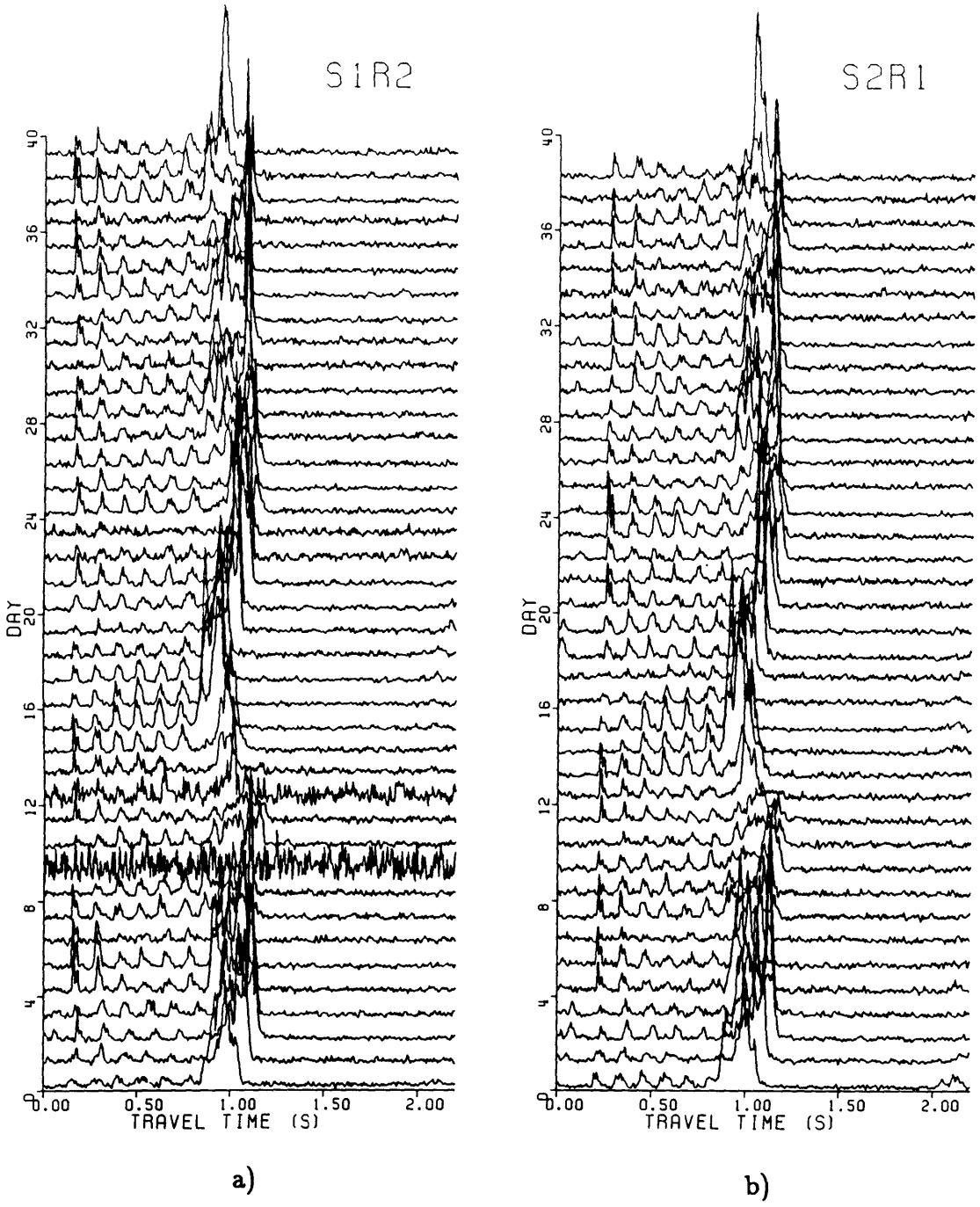

Figure 2.11. Daily averaged pulse responses for (a)S1R2, (b)S2R1, (c)S1R3, (d)S3R1, (e)S2R3, and (f)S3R2

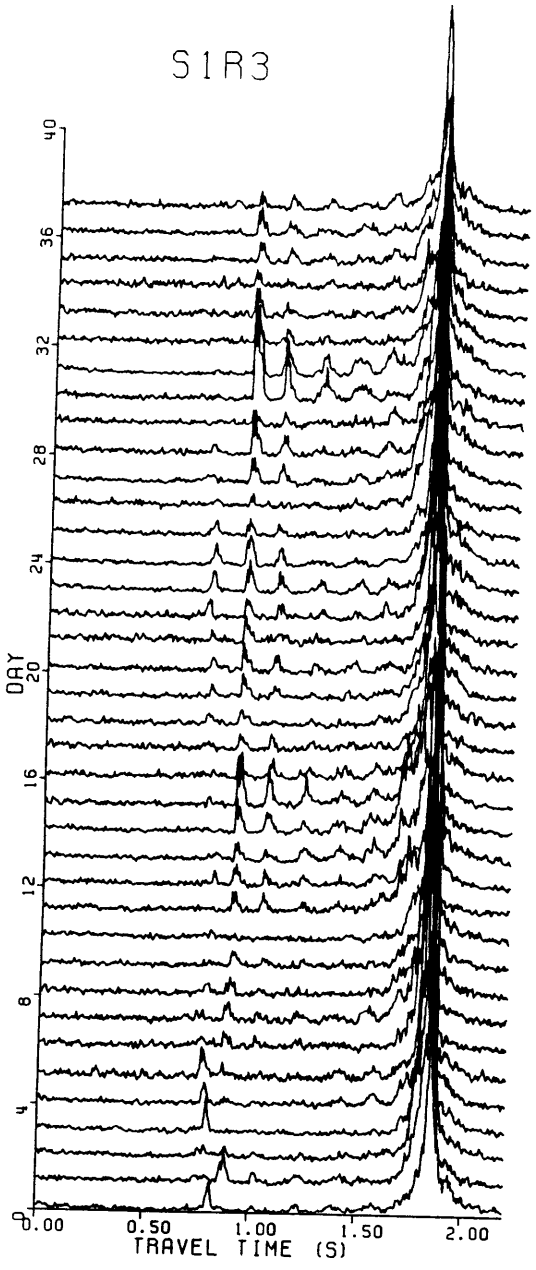
S1R3
DAY
0
4
8
12
16
20
24
28
32
36
40
0.00
0.50
1.00
1.50
2.00
TRAVEL TIME (S)

c)

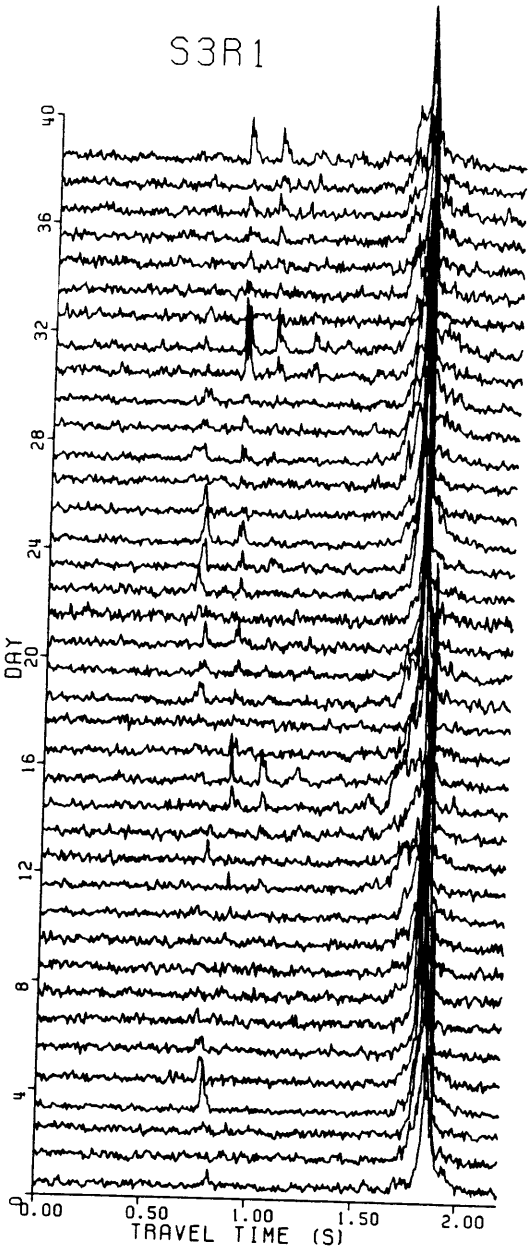
S3R1
DAY
0
4
8
12
16
20
24
28
32
36
40
0.00
0.50
1.00
1.50
2.00
TRAVEL TIME (S)

d)

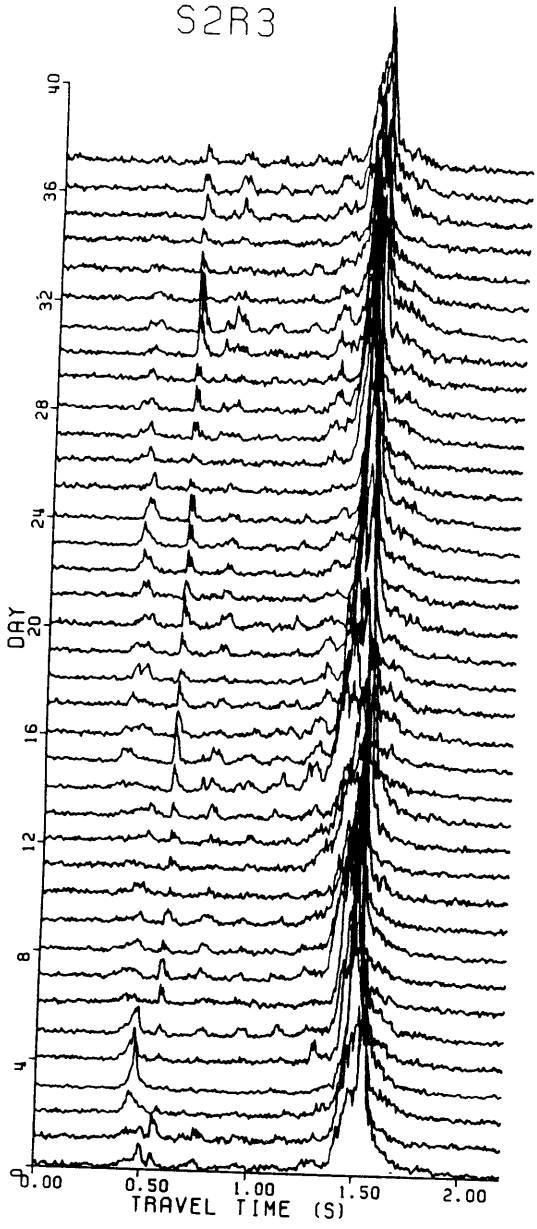
S2R3
DAY
TRAVEL TIME (S)
0.00
0.50
1.00
1.50
2.00
4
8
12
16
20
24
28
32
36
40

e)

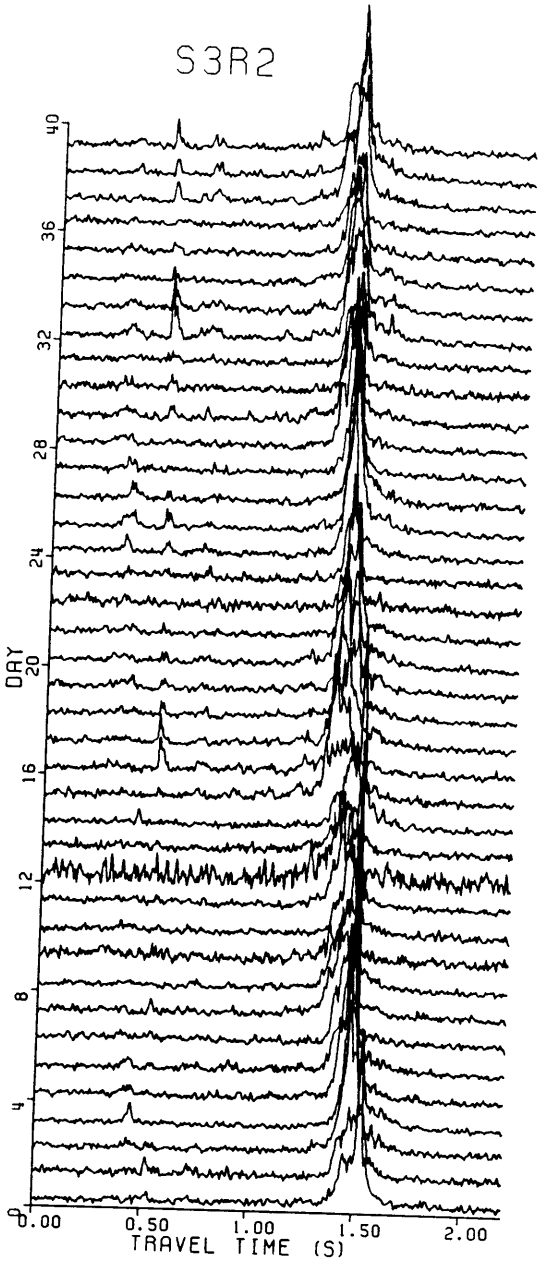
S3R2
DAY
TRAVEL TIME (S)
0.00
0.50
1.00
1.50
2.00
4
8
12
16
20
24
28
32
36
40

f)

time and easily identified. A very small percentage of the processed data (less than 5 percent) had to be edited to remove high ambient noise levels. Also, if a pulse could not be identified above the background noise, the travel time was interpolated from the previous and later corresponding arrivals. The same procedure was applied to the pulse responses of S1R3, S3R1, S2R3, and S3R2. The precursor pulse arrivals for these four records showed less stability, thereby complicating the identification process. More of the pulse response data (approximately 25 percent) needed editing. It should be noted that a gross misidentification of an arrival time will show up in the output of the inversion as an unrealistic oceanographic fluctuation. On the other hand a slight error in arrival time estimation may be falsely interpreted as an oceanographic signal which does not really exist. Applying an error to the measured data (pulse arrival time) in the inversion is used to mitigate this problem.

The precision of travel time resolution has significant implications. Temperature variations cause the largest fluctuations in pulse travel time. A temperature deviation of 2°C corresponds to a change in travel time of about 200 ms (for a 45 km range). Current induced fluctuations in travel time are much smaller. A 50 cm/s current (acting over a 45 km range) will alter the travel time by only 10 ms. So an uncertainty of 5 cm/s in current velocity is the maximum precision attainable for a travel time error of 1 ms.

The estimation of travel time variance is not a simple task. The major source of error is insufficiently resolved rays which arise due to multipath interference. Internal wave related variance is the next most important random error, with errors in the signal processing being minimal. From the 1983 reciprocal tomography experiment (which was conducted near Bermuda), the internal wave induced variance was estimated to be about 10 ms^2 (see Stoughton et al., 1986). The transmission range for the 1983 reciprocal tomography experiment was 300 km, which is much longer than the 45 km range of the Florida Straits experiment. The internal wave

induced variance is directly related to the rms phase delay along the ray path, which is roughly proportional to range (see Flatte et al., 1979). We thus expect a smaller variance due to internal wave effects in the Florida Straits experiment due to the much shorter transmission range. DeFerrari and Nguyen (1986) were able to resolve tidal currents in the Florida Straits from the small triangle tomography experiment, and estimated the total rms travel time error for the experiment to be about 0.2 ms. The small triangle experiment had a transmission range of roughly 25 km, and a quicker transmission rate (a complete cycle of reciprocal transmissions took place every 12 minutes). Table 3 gives the estimated travel time variance for this experiment. The daily averaged travel time is estimated to have an rms error of about 1 ms.

Table 3: Travel Time Variance

Matched filter receiver precision (σ_τ variance) $\sigma_\tau = [2\pi(\delta f)_{rms}(\frac{2E}{N})^{\frac{1}{2}}]^{-1}$	0.07 ms^2
Interpolation error variance	0.05 ms^2
Internal wave related variance	5 ms^2
Interference related variance	10 ms^2
Total variance	15 ms^2
Daily mean variance	$\sim$ 1 ms^2
Daily averaged rms travel time error	$\sim$ 1 ms

Errors arising from mooring motion and clock timing have not yet been addressed. The transceivers for this experiment were moored 38 meters above the bottom. If we assume a 1 m/s current acting on the entire mooring, a maximum horizontal displacement of 0.5 meters is estimated (DeFerrari and Nguyen, 1986).

This change in ray path length would correspond to a maximum travel time error of 0.3 ms. Clock drift is a nonreciprocal error which is due to a clock at one of the units being fast relative to a clock at another unit. Correcting clock timing errors is usually accomplished by a linear detrending of the clock drift referenced to a more precise standard clock. Unfortunately, the final clock readings were not obtained during this experiment. This does not present a problem in the estimation of temperature and vorticity as the clock errors cancel with reciprocal transmissions. But the clock error does not cancel in the estimation of the current. This issue will be discussed in Section 5.2 when we consider the estimation of current in more detail.

Chapter 3

Ocean Acoustics and the Forward Problem

3.1 Ray Theory

The forward problem of modelling acoustic propagation in an oceanic waveguide can be attacked in several manners, all of which involve solving the wave equation. Perhaps the simplest and most physically insightful method is a development in terms of acoustic rays, which have a direct analogue in the field of optics. Implicit in the ray theoretical approach is the assumption that the refractive properties of the medium change only slightly over an acoustic wavelength (this is geometrical optics, or the WKB approximation). Snell's law of refraction is the result of this formulation, and the paths of energy propagation through the medium are explicitly specified. But ray theory is not an exact solution for the acoustic wavefield, and as such does not account for diffraction and other wave effects. Nevertheless, ray theory was chosen for this analysis due to the simplicity of matching pulse arrival times with ray theoretical predictions and the ease of constructing the inverse operator (ray path spatial coverage).

Before proceeding, two other theoretical approaches to solving the wave equation should be mentioned. Normal mode theory gives an exact solution to the wave equation based on the preferred vibrations (normal modes) of the waveguide. The normal mode picture becomes complicated when the medium is range dependent

(due to irregular bathymetry and/or strong inhomogeneities such as fronts or eddies), and mode coupling must be considered. A second approach, the parabolic equation method, is based on the paraxial (small angle) approximation to the wave equation. The result is a model which is very useful for modelling propagation in a range dependent waveguide.

A development of the solution to the wave equation in terms of rays is now given. We follow in similar fashion to a derivation found in Tolstoy and Clay (1966). Other good references include Officer (1958) and Brekhovskikh and Lysanov (1982). The wave equation is given by

$$\nabla^2 p \; - \; \frac{1}{c^2}\frac{\partial^2 p}{\partial t^2} \; = \; 0 \; , \tag{3.1}$$

where p is the acoustic pressure and c is the sound velocity, which may vary with the spatial coordinates (i.e., $c \; = \; c(x,y,z)$). For a harmonic source $e^{-i\omega t}$, the wave equation becomes the Helmholtz equation

$$\nabla^2 p \; + \; k^2 p \; = \; 0 \; , \tag{3.2}$$

with k being the wavenumber in the direction of propagation. We rewrite the wavenumber k as

$$k \; = \; \frac{\omega}{c} \; = \; \frac{\omega}{c_o}\frac{c_o}{c} \; = \; k_o n \; , \tag{3.3}$$

where c_o is a constant reference sound velocity and $n \; = \; \frac{c_o}{c}$ is the index of refraction. Without loss of generality we represent the acoustic pressure as

$$p \; = \; A e^{ik_o S(x,y,z)} \; , \tag{3.4}$$

where A is the wave amplitude and $k_o S$ is the phase of the wave. Substituting (3.4) into (3.2), and collecting real and imaginary terms, we are left with two equations:

$$\nabla^2 A \; - \; k_o^2 A \, [n^2 \; - \; (\nabla S)^2] \; = \; 0 \; , \tag{3.5}$$

and

$$2 \nabla A \cdot \nabla S \; + \; A \nabla^2 S \; = \; 0 \; . \tag{3.6}$$

Up to this point the equations are exact solutions to the wave equation.

We now follow in the footsteps of ray optics and make the assumption

$$\frac{\nabla^2 A}{k^2 A} \; << \; 1 \; . \tag{3.7}$$

A strict interpretation of this assumption is that the rate of variation of the wave phase (per wavelength) of the vertical component of wavelength is small (see Tolstoy and Clay (1966)). More generally, the fractional change in the sound speed gradient $(\frac{dc}{dz})$ must be small in comparison with the gradient $\frac{c}{\lambda}$, where λ is the acoustic wavelength. Simpler yet, the propagating medium must vary only slightly over an acoustic wavelegth.

Applying this condition (Equation (3.7)) to Equation (3.5), we then have

$$(\nabla s)^2 \; = \; n^2 \; , \tag{3.8}$$

or writing out the operator

$$(\frac{\partial S}{\partial x})^2 \; + \; (\frac{\partial S}{\partial y})^2 \; + \; (\frac{\partial S}{\partial z})^2 \; = \; n^2 \; . \tag{3.9}$$

This is the eikonal equation, and the cornerstone of ray theory. A physical picture of rays follows direcly from the solutions to the eikonal equation. Surfaces of constant phase (wave fronts) are given by S = constant, and the orthogonals to the wave fronts (∇S) define the rays. The rays represent the paths along which acoustic energy is propagated. The amplitude of the rays is given by Equation (3.6), which is often referred to as the transport equation. It should be noted that the eikonal equation is not necessarily a solution to the wave equation due to the geometrical optics approximation.

We now wish to parameterize the acoustic rays in terms of the refractive properties of the medium. The formulation of the ray path equations follows directly from the eikonal equation, and is presented here for completeness. The unit vector along a ray (normal to an S = constant surface) is given by

$$n\frac{dr}{ds} = \nabla S \,, \tag{3.10}$$

where $r = r(x,y,z)$ and s is the arc length along the ray. Differentiating along a ray path ($\frac{d}{ds}$), and using the eikonal equation and Equation (3.10), we obtain

$$\frac{d}{ds}(n\frac{dr}{ds}) = \nabla n \,. \tag{3.11}$$

This equation describes the ray trajectories in terms of the index of refraction $n = n(x,y,z)$. Rewriting (3.11) in component form,

$$\frac{d}{ds}(n\frac{dx}{ds}) = \frac{\partial n}{\partial x} \,, \tag{3.12a}$$

$$\frac{d}{ds}(n\frac{dy}{ds}) = \frac{\partial n}{\partial y} \,, \tag{3.12b}$$

$$\frac{d}{ds}(n\frac{dz}{ds}) = \frac{\partial n}{\partial z} . \tag{3.12c}$$

These equations are often called the ray path equations, and are a generalization of Snell's law.

It should be noted that the ray paths satisfy Fermat's principle. The time of arrival of a ray is given by the integral

$$\tau = \int_\Gamma \frac{ds}{c} , \tag{3.13}$$

where ds is arc length along the ray and Γ represents the ray path. Fermat's principle states that the travel time along a ray path is an extremum (i.e., $\delta\tau = 0$). In real physical space a ray represents a path of stationary time, and the travel time is given by the minimum value. The ray path equations, along with Fermat's principle, allow us to trace rays through a medium varying in all three directions (i.e., $c = c(x, y, z)$).

For most practical cases of ray tracing, we consider propagation in the vertical plane with the sound speed a function of depth only (i.e., $c = c(z)$). This is a good approximation due to the vertically stratified nature of the oceanic waveguide. So if we consider propagation in the $r - z$ plane, where r is horizontal range, our ray path Equations (3.12) become

$$\frac{d}{ds}(n\frac{dr}{ds}) = \frac{\partial n}{\partial r} = 0 , \tag{3.14}$$

$$\frac{d}{ds}(n\frac{dz}{ds}) = \frac{\partial n}{\partial z} = \frac{dn}{dz} . \tag{3.15}$$

From Equation (3.14a) we see that

$$n\frac{dr}{ds} = constant . \tag{3.16}$$

If we take θ as the angle which the ray makes with the vertical, then $\frac{dr}{ds} = \sin\theta$, and we arrive at

$$n \sin\theta = \frac{\sin\theta}{c} = p\ (constant)\ . \tag{3.17}$$

This is Snell's law, and can be considered a statement of the conservation of the horizontal component of the wavenumber along a ray path when $c = c(z)$. It is a very useful relation as it allows us to trace the refraction (bending) of ray paths through a variably refracting medium. The ray parameter p is constant along a given ray path but varies from one ray to another. It is also useful to note that for the case of a constant sound speed gradient (linear $c(z)$ profile), the rays trace out arcs of a circle.

Most ray tracing programs use constant sound speed gradient segments to approximate a continuous sound speed profile. Different sound speed profiles can be specified at various ranges for the range dependent case. Interpolation between successive locally range independent sound speed profiles gives the sound speed as a function of range. The ray paths are then calculated by integration of the ray path equations (as specified by Snell's law). The ray is assumed to travel in a vertical plane connecting the source and receiver. Out of plane effects which produce horizontal sound speed gradients are assumed to be small. The sound speed profiles are such that only a few ray paths actually connect a given source and receiver. These paths are called eigenrays. Ray tracing programs typically send out a fan of rays (with slightly offset launch angles), and march along in range in accordance with Snell's law to the range of the receiver. The eigenrays are then the paths which 'hit' the receiver.

Brief mention is now made of two of the problems encountered during ray tracing. Firstly, by dividing the sound speed profile into segments of constant sound speed gradient, we are left with discontinuities in $\frac{dc}{dz}$. These discontinuities may lead to a spurious focusing effect, often referred to as a false caustic. This problem may be alleviated by using curved line segments to approximate the velocity profile. Secondly, ray theory (geometric optics) is, in principle, a no reflection theory. Corrections need to be applied at caustics and turning points. This can be accomplished by keeping more terms in the WKB approximation.

In this analysis, we use the range dependent eigenray program MPP (multiple profile ray tracing program) developed by C. W. Spofford. The sound speed field is linearly interpolated in both depth and range in specified triangular sectors. The bottom bathymetry is represented by piecewise linear segments. Output of the program includes eigenray arrival times and transmission loss (calculated form geometrical spreading and losses due to boundary reflections), along with a history of the eigenray trajectories.

3.2 Ray Arrivals in Shallow Water

Acoustic propagation in the ocean is intimately related to the structure of the sound speed profile. Sound speed may be calculated with the simple equation (Medwin, 1975)

$$c = 1449.2 + 4.6T - 0.055T^2 + 0.00029T^3 + (1.34 - 0.010T)(S - 35) + 0.016z \tag{3.18}$$

where c is the speed (m/s), T is the temperature (°C), S is the salinity (ppt), and z is the depth (m). From this relation we see that the velocity of sound is primarily a

function of temperature and pressure, with salinity being of secondary importance under general oceanic conditions.

Three different cases of acoustic propagation are illustrated in Figures 3.1. Figure 3.1a demonstrates acoustic propagation in the deep ocean. The deep ocean typically has a sound speed profile which has a minimum (sound channel axis) at roughly 1000 m. The high speed at the surface can be attributed to warm temperatures, while high sound speed at depth is a consequence of the increasing pressure. The result is a highly refractive acoustic waveguide which is conducive to long wave propagation. A shallow water waveguide with no surface mixed layer is shown in Figure 3.1b. Propagation in this case is limited to bottom interacting rays due to the downward refractive nature of the sound speed profile. Figure 3.1c illustrates the case of a shallow water waveguide with a surface mixed layer. In this example, the mixed layer acts as a surface duct and traps rays which penetrate near the surface. Rays which have turning depths below the mixed layer are unaffected by the surface duct and follow paths similar to those found in Figure 3.1b.

We now proceed to the ray tracing for the October 1983 tomography experiment. Averaged Pegasus profiler temperature/pressure data for stations 3a - 7 (see Figure 2.4 for Pegasus station locations), along with a climatological temperature-salinity relationship, was used for the computation of the sound speed profiles for the region. All of the sound speed profiles are similar in structure (see Figure 3.2). Each exhibits a near constant velocity surface layer to a depth of almost 100 meters, and then a decrease in sound velocity with depth. We therefore expect (see Figure 3.1c) both surface ducted eigenrays and downward refracted bottom interacting eigenrays.

Range independent ray traces are presented in Figures 3.3a,b for transmission along the north/south leg of the array (S1R2) and the lower leg (S1R3), respectively. The sound speed profile from Pegasus station 3a is used as the reference profile in

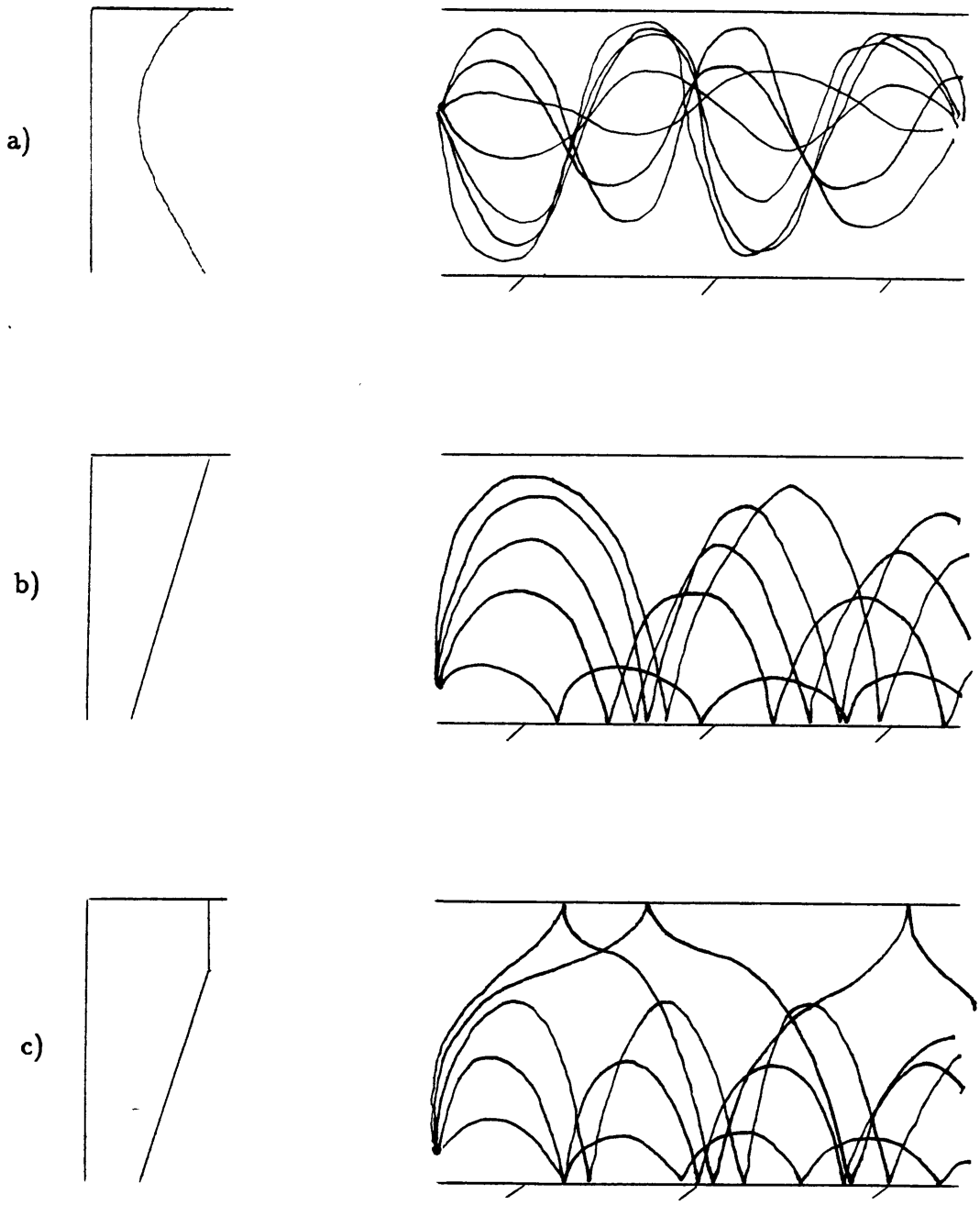

Figure 3.1. Acoustic propagation in the ocean - (a)the deep sea, (b)shallow water with no mixed layer, and (c)shallow water with a mixed layer.

the S1R2 case, and the average profile of Pegasus stations 3a - 7 is used for the S1R3 case. The bottom depth is constant for both cases, and represents the average along the leg (as obtained by interpolation of the bathymetric chart of Malloy and Hurley (1970)). Transceivers are moored 38 meters above the bottom. Only the eigenrays with less than six surface reflections are shown. The flat bottom range independent

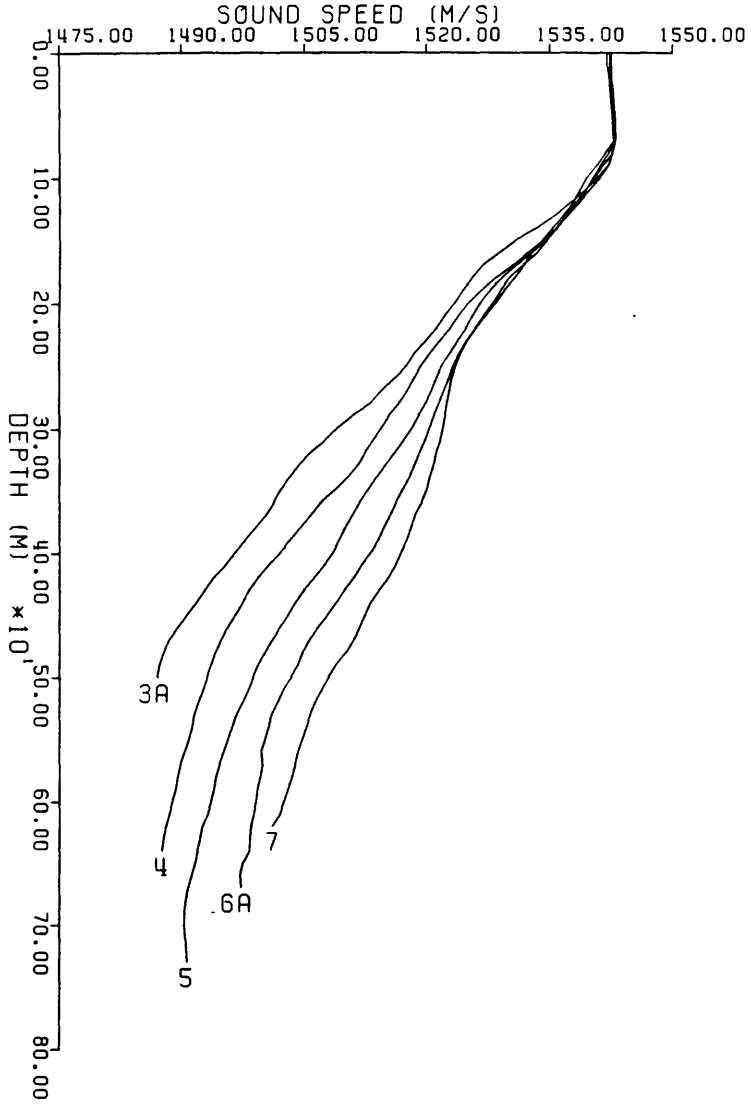

Figure 3.2. Sound speed profiles computed from Pegasus profiler temperature/ pressure data for stations 3a-7.

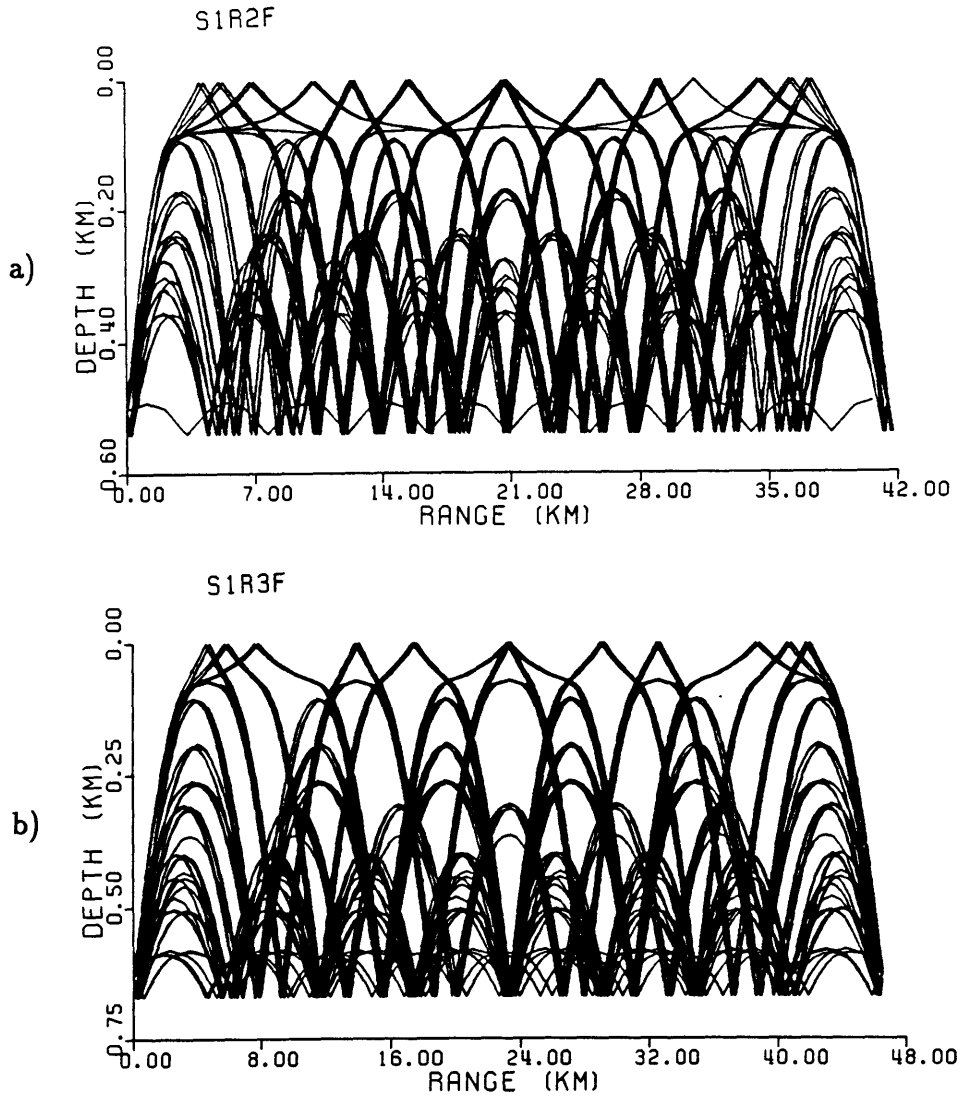

Figure 3.3. Range independent ray traces for transmission along (a)the north/south leg of the array (S1R2 or S2R1), and (b)the lower leg (S1R3 or S3R1).

case is symmetric, so sources and receivers may be interchanged. Thus, Figure 3.3a is representative of both S1R2 and S2R1. Similarly, Figure 3.3b is representative of both S1R3 and S3R1, and also S2R3 and S3R2 since the leg separations and averaged bottom depth are almost the same for the upper and lower legs of the triangle.

Several features of the range independent ray traces are worth mentioning. Surface ducted rays (SD) are evident in both Figures 3.3a,b, although more dramatic along the the north/south leg (S1R2, S2R1). An abundance of refracted, bottom reflected rays (RBR) is seen in both cases. A typical lobe distance (distance between successive bottom bounces) is on the order of 5 kilometers for the two cases. Also note that the ray tracing plots are vertically exaggerated. The steepest eigenray has an initial source angle with respect to the horizontal of 16°.

The ray tracing picture is not complete without a discussion of the arrival sequence of eigenrays. Figures 3.4a,b are plots of eigenray travel time versus relative intensity for the range independent flat bottom cases S1R2 and S1R3, and correspond to Figures 3.3a,b, respectively. We first consider the eigenrays associated with the north/south leg (S1R2, S2R1) of the triangle (see Figure 3.4a). The first five sets of arrivals correspond to surface ducted rays, with the first set (at 27.15 s) comprising rays which have two turning points in the surface duct (2SD). The second set of arrivals (at 27.27 s) consists of 3SD rays, the third set (at 27.40 s) of 4SD rays, the fourth set (at 27.52 s) of 5SD rays, and the fifth set (at 27.64 s) of 6SD rays. The large clump of eigenrays which arrive from 27.70 s to 27.90 s represent the RBR rays. The remaining eigenray arrivals ($>$ 27.90 s) correspond to surface reflected rays with more than six surface reflections. A similar picture evolves for the range independent flat bottom case S1R3 (or S3R1, S2R3, S3R2), although the 1SD and 2SD arrivals are absent (see Figure 3.4b).

The eigenray travel time is a function of both path length and sound speed. From the eigenray arrival sequences, it is seen that rays travelling in the higher sound velocity surface layer arrive earlier than the RBR rays despite a longer path length. This trend can also be observed in a plot of eigenray travel time as a function of initial angle (see Figure 3.5 for the S1R2 case). The eigenrays with larger initial

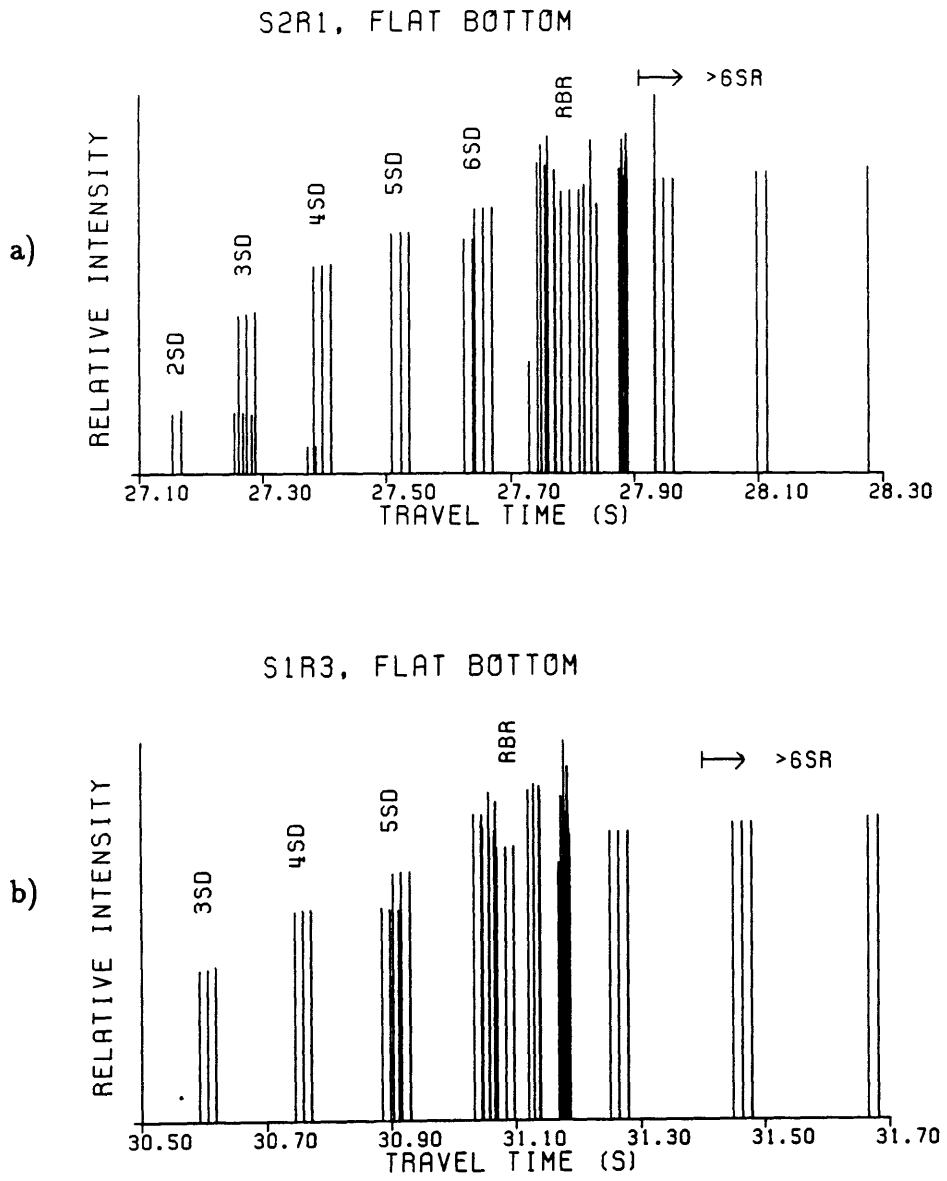

Figure 3.4. Eigenray arrival time versus relative intensity for the range independent flat bottom cases (a)S1R2 or S2R1, and (b)S1R3 or S3R1.

angle (SD rays) arrive earliest, up to the point where the ray path length takes over for rays with a large number of reflections at 27.75 s. The RBR arrivals, with initial angles ranging from -13° to 13°, all arrive at nearly the same time (27.9 s).

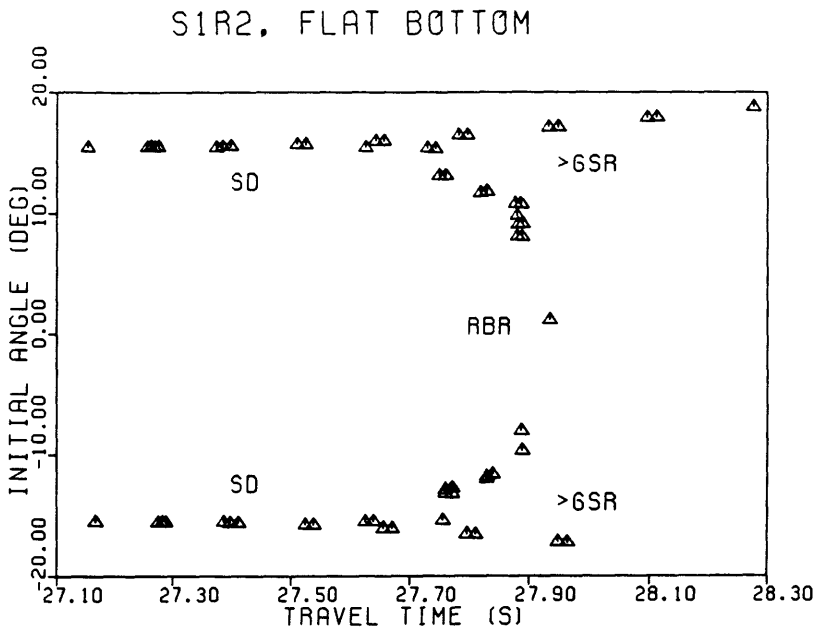

Figure 3.5. Order of ray arrivals.

A few comments about the relative intensities calculated by the model should be made at this point. Transmission loss is dominated by spherical spreading. No effort was made to correctly parameterize bottom loss in this study due to the complicated bathymetry. From ideal reflection theory, the critical angle for the seabed interface is estimated at about 30° (from the horizontal). All of the traced eigenrays intersect the bottom at angles less than critical, and suffer no loss according to ideal reflection theory. In the real ocean, experimental data suggests that bottom loss is roughly 2 db per bottom bounce for the angles of interest and an acoustic frequency of 460 Hz. Surface loss is smaller and can be estimated at about 0.5 db loss per surface reflection. A more detailed account of the various propagation losses which are responsible for the shaping of the RBR pulse arrival peak for the August 1983 tomography experiment is given by Monjo (1987). In this

analysis we are more concerned with obtaining an accurate travel time estimate for the pulse arrival time as our inverse scheme does not incorporate amplitude data. Brown (1982) does a waveform inversion (using both phase and amplitude information) with synthetically generated arrivals and does not obtain a significant improvement in inverse results in comparison with a 'travel time only' inversion. The pulse arrival time (phase) is a more robust datum in the context of ray theory. Internal wave and multipath interference have a lesser effect on travel times than on the acoustic amplitude.

We now present the range dependent ray traces (with irregular bathymetry, but a range independent sound speed profile). Using range dependent sound speed profiles did not change the results very much due to the similarity of the sound speed profiles in the region (see Figures 3.2). The eigenray plots for all six cases are shown in Figures 3.6a-f, with the corresponding eigenray arrival sequences given in Figures 3.7a-f. Note that the bathymetry along leg 1-2 is very gentle in comparison with the other two legs. The ray tracing results for S1R2 and S2R1 (Figures 3.6a,b) are very similar to the results obtained in the range independent case. However, looking at the associated travel time plots (Figures 3.7a,b), we see that the two earliest SD ray arrivals are now missing. The ray traces for the legs 1-3 and 2-3 of the triangle (Figures 3.6c-f) show a much greater change from the range independent case due to interactions with the highly irregular bathymetry. All four cases (see Figures 3.7c-f) show a collection of RBR arrivals bunched together, with some precursor SD arrivals.

The range dependent results must be qualified. We recognize that the bottom topography is rather speculative and may be in error by tens of meters. Palmer et al., (1985) find that the identification of eigenrays in the Florida Straits becomes

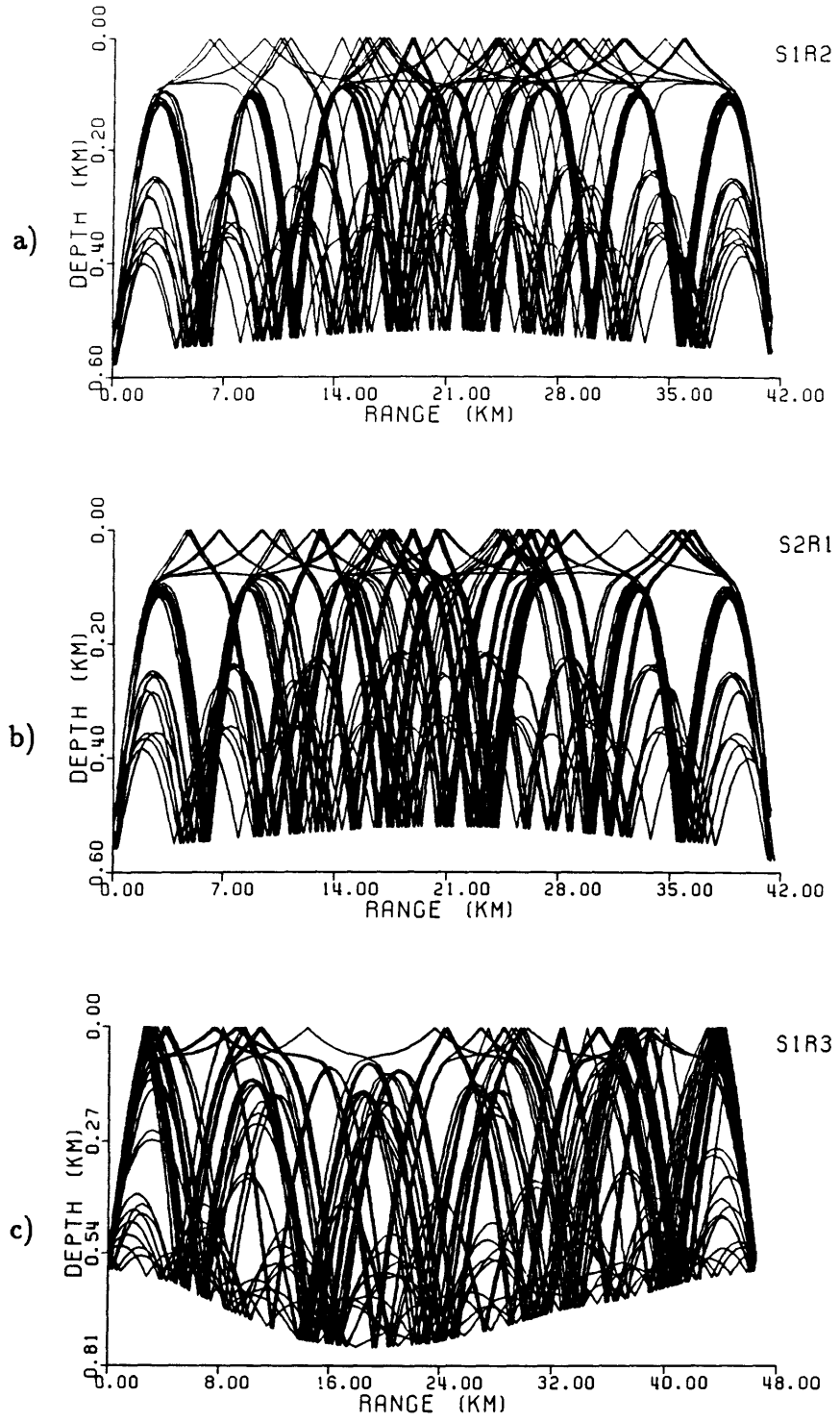

Figure 3.6. Range dependent ray traces for (a)S1R2, (b)S2R1, (c)S1R3, (d)S3R1, (e)S2R3, and (f)S3R2.

d)

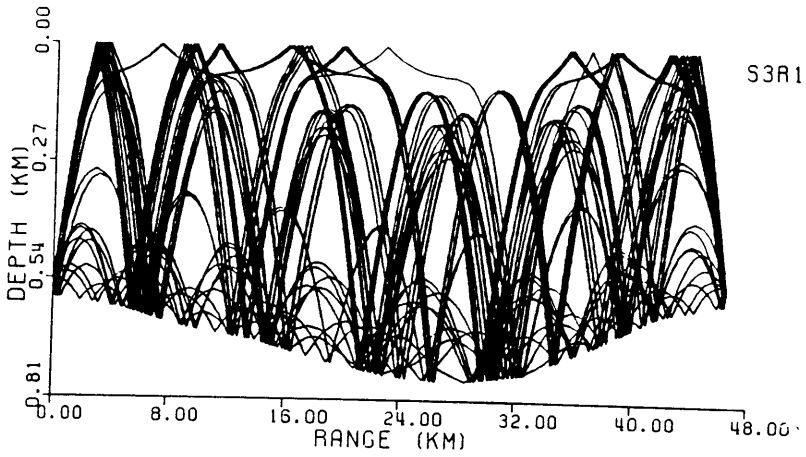
S3R1
DEPTH (KM)
0.00
0.27
0.54
0.81
0.00
8.00
16.00
24.00
32.00
40.00
48.00
RANGE (KM)

e)

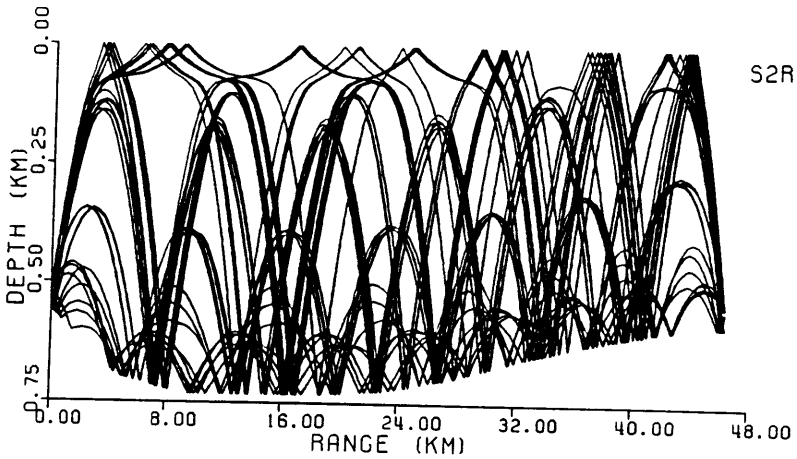
S2R3
DEPTH (KM)
0.00
0.25
0.50
0.75
0.00
8.00
16.00
24.00
32.00
40.00
48.00
RANGE (KM)

f)

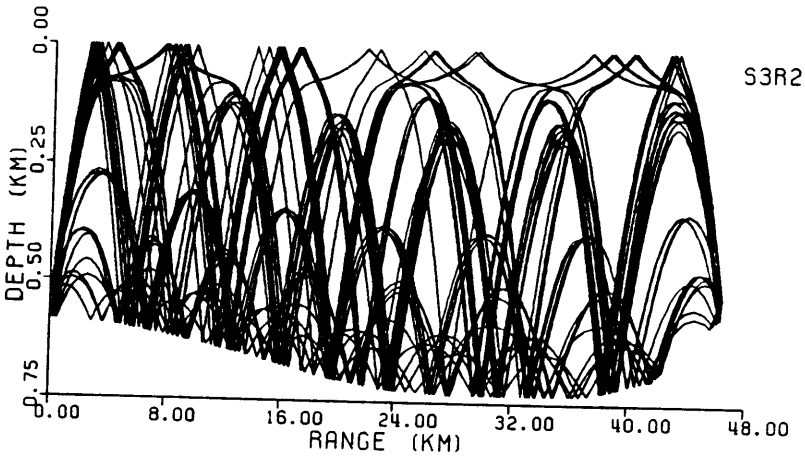
S3R2
DEPTH (KM)
0.00
0.25
0.50
0.75
0.00
8.00
16.00
24.00
32.00
40.00
48.00
RANGE (KM)

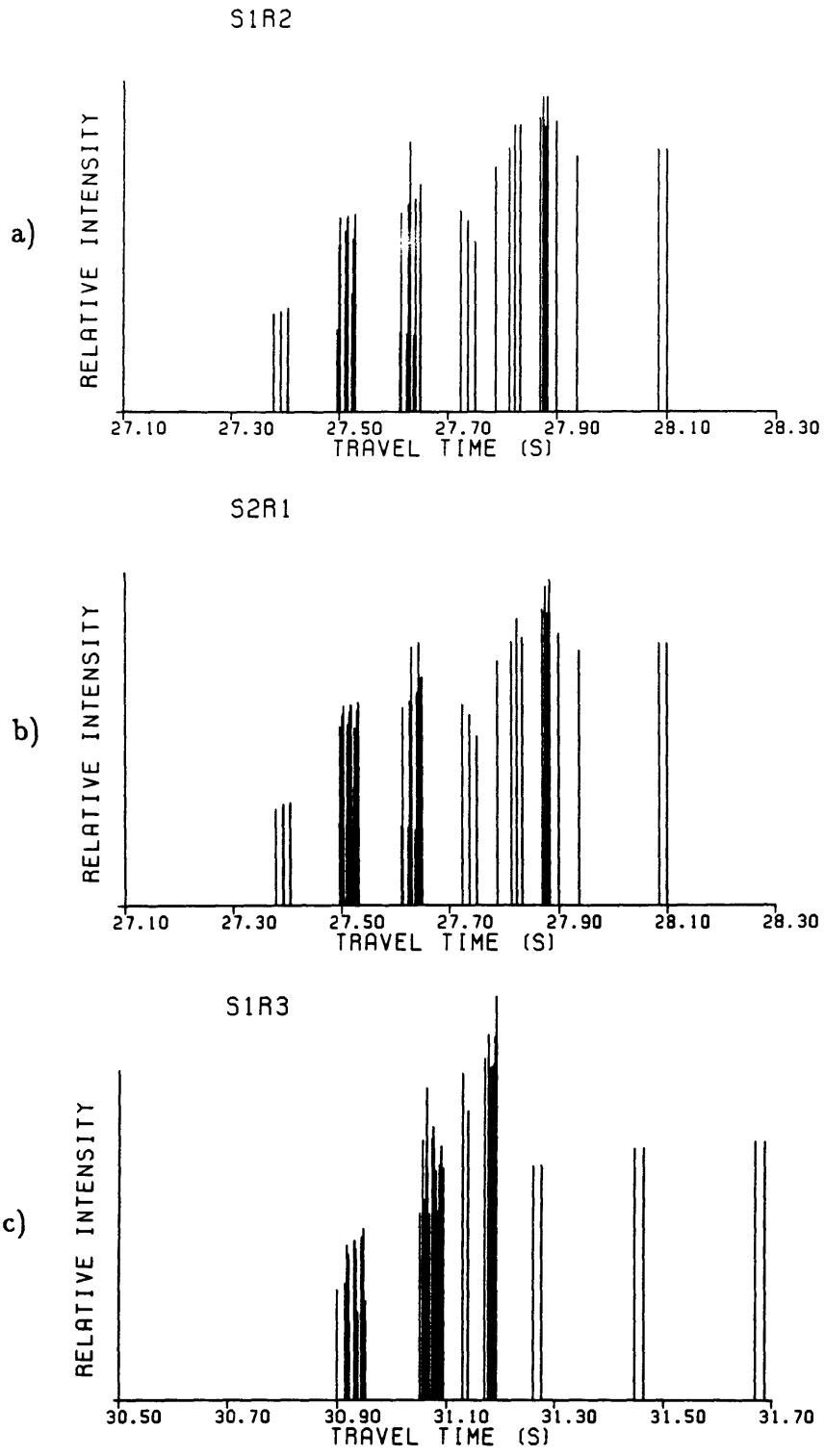

Figure 3.7. Eigenray arrival sequences for (a)S1R2, (b)S2R1, (c)S1R3, (d)S3R1, (e)S2R3, and (f)S3R2.

d)

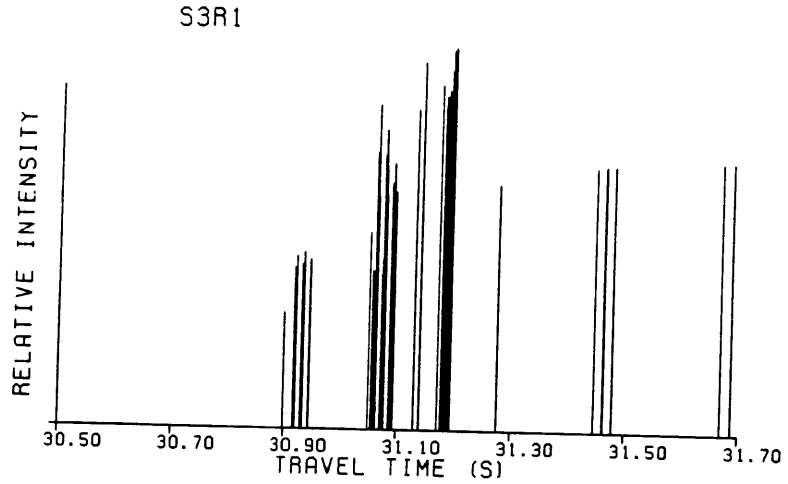
S3R1
RELATIVE INTENSITY
30.50
30.70
30.90
31.10
31.30
31.50
31.70
TRAVEL TIME (S)

e)

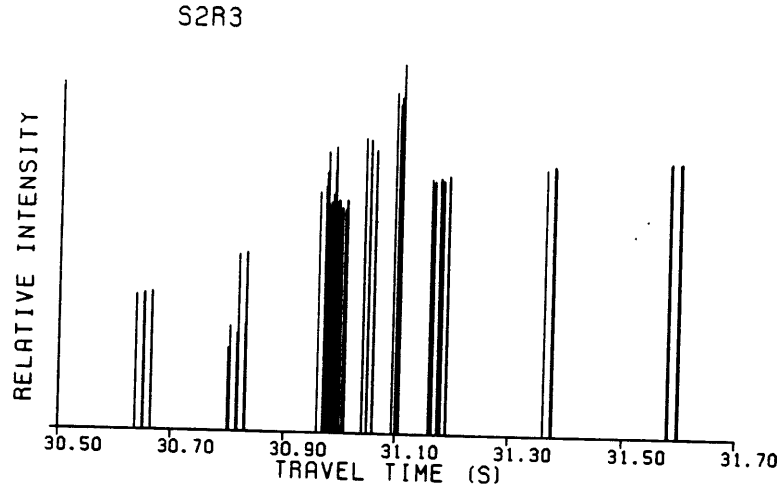
S2R3
RELATIVE INTENSITY
30.50
30.70
30.90
31.10
31.30
31.50
31.70
TRAVEL TIME (S)

f)

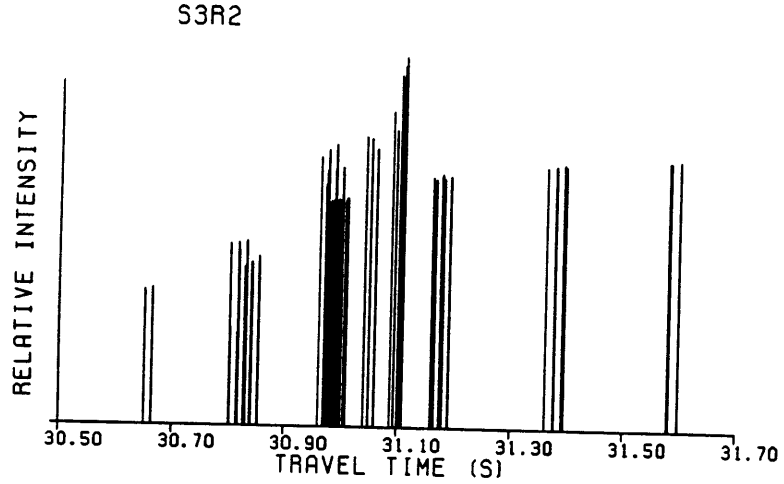
S3R2
RELATIVE INTENSITY
30.50
30.70
30.90
31.10
31.30
31.50
31.70
TRAVEL TIME (S)

nearly impossible after only a few bottom bounces due to small perturbations in bathymetry. The range dependent ray traces are presented mainly to illustrate the similar features which exist in both the range dependent and range independent cases.

The next step is to match the travel times of the pulse response data with the arrival times predicted by ray theory. The pulse response data was already presented in Figures 2.11a-f. We first look at the identification of the peaks in S1R2. Figure 3.8a matches a typical daily averaged S1R2 pulse response record with the arrival sequence of the calculated eigenrays in the range independent flat bottom S1R2 case. The main (latest arriving) peak in the pulse response record corresponds to the large cluster of RBR arrivals. Five of the precursor SD arrivals can be identified in comparison with the ray trace. The exception is the first precursor arrival in the pulse response record which has no match. This peak probably corresponds to a ray which is surface ducted and hits the receiver en route to its first bottom bounce. This belief is supported by the fast travel time and the relative spacing of this peak in relation to the other SD arrivals. A ray of this nature is highly diffracted, and this may explain why it is not seen in the ray trace. This ray is effectively a 1SD ray. The remaining arrivals predicted by ray theory which have no match with the pulse response record are rays with numerous boundary reflections whose transmission loss was inadequately accounted for. These arrivals are not seen in the pulse response data as they are below the noise level. The same identification follows for the reciprocal transmission S2R1.

Identification of the S1R3 pulse response peaks is more difficult (see Figure 3.8b). The main peak still corresponds to the large clump of arrivals, but the pulse response SD precursor arrivals have no match with the ray theoretical predictions. The shape of this peak, with a steep leading edge, is very much like the 1SD peak in S1R2. Also, the fast arrival time (in comparison with the main peak) in-

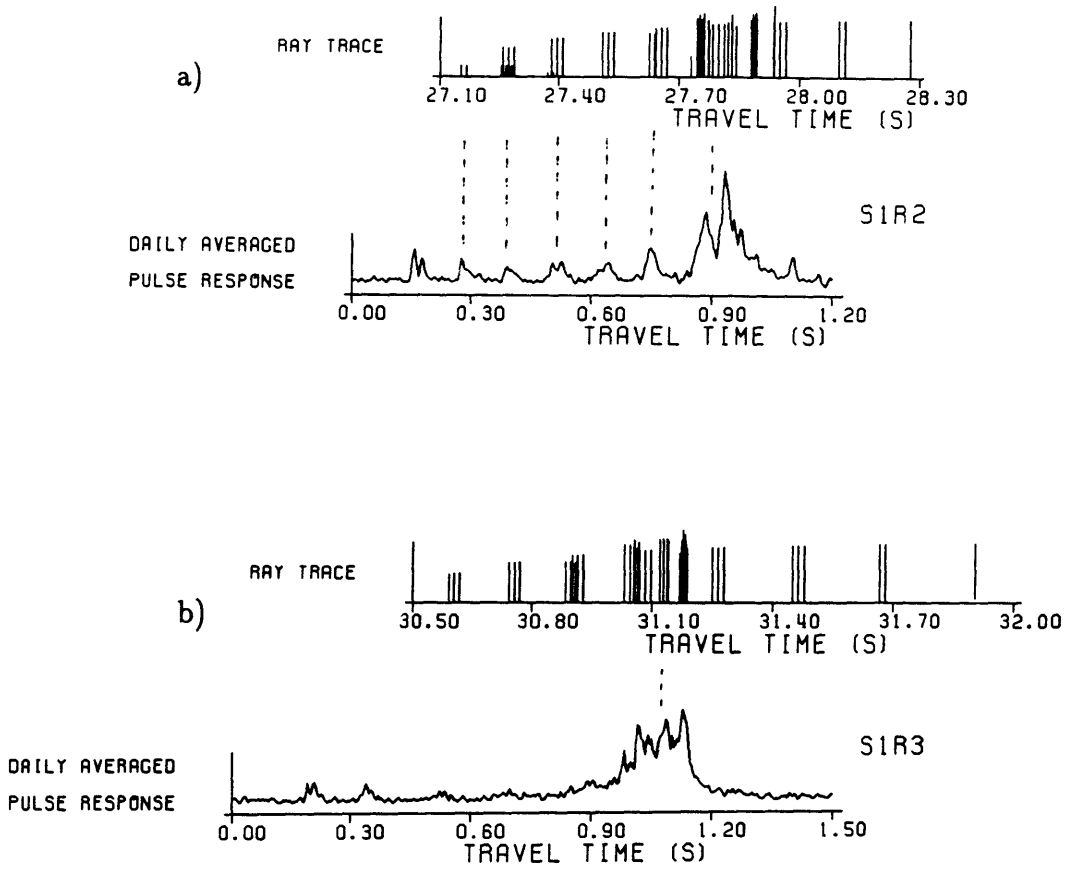

Figure 3.8. Peak identification for (a)S1R2 and (b)S1R3.

dicates propagation in the high velocity surface duct. By analogy with the S1R2 case, we take this arrival as being effectively a 1SD ray. The second ray (which is not always identifiable) similarly corresponds to a 2SD ray. The same identification follows for S2R3, S3R1, and S3R2. Several of the pulse responses show a broader peak which arrives even earlier than the 'identified' 1SD (see, for example, day 25 of Figure 2.11f). The presence of this peak is not understood at this time.

3.3 Formulation of the Forward Problem

The forward problem in acoustic tomography describes the dependence of the pulse travel time along a particular path on the sound speed field of the ocean. The travel time along a ray path is given by

$$T_i = \int_{\Gamma_i} \frac{ds}{c(\mathbf{x},t) + \mathbf{u}(\mathbf{x},t)\cdot\tau}, \tag{3.19}$$

where c is the sound speed field, $\mathbf{u}$ is the current component along the ray, s is arc length along the ray, and τ is a unit vector tangent to the ray. The travel time of a given ray is dependent upon the path length, sound speed, and current velocity along the ray path. Variations in sound speed and current will lead to deviations in travel time, along with a change in the ray path. Hamilton et al., (1980) show that there is a negligible change in travel time associated with this change in path length. But the change in path length leads to a different sampling of the oceanic medium. It is assumed (and usually valid) that the ray path in the perturbed medium is almost identical to that in the unperturbed medium. One can check the validity of this assumption a posteriori by tracing the ray path in the sound speed field calculated by the inverse, and then comparing with the path traced in the unperturbed medium.

The size of the terms in the denominator of the integrand of (3.18) are now examined more closely. Values characteristic of the Florida Straits region are used in the following arguments. A typical current speed is $u = 50$ cm/s and a typical sound speed is $c = 1500$ m/s, so $\frac{u}{c} = O(10^{-3}) << 1$. Typical values for the vertical shear of current and sound speed are $\frac{du}{dz} = \frac{10\text{cm/s}}{100\text{m}} = O(10^{-3})$ and $\frac{dc}{dz} = \frac{5\text{m/s}}{100\text{m}} = O(10^{-2})$, so $\frac{dc}{dz}$ is at least one order of magnitude larger than $\frac{du}{dz}$. This

simple scaling analysis shows that the refraction of rays is dominated by the sound speed gradient, and that the current can be ignored in ray tracing simulations.

The travel time path integral (3.18) is nonlinear in the sound speed field, so we linearize about a reference state. The sound speed is written as

$$c(\mathbf{x},t) \;=\; c_o(\mathbf{x},t_o) \;+\; \delta c(\mathbf{x},t)\;, \tag{3.20}$$

where c_o is a reference sound speed field and δc is the deviation from the reference field. Also,

$$\delta c(\mathbf{x},t) \;<<\; c_o(\mathbf{x},t_o)\;. \tag{3.21}$$

Substituting (3.19) into the travel time path integral (3.18)

$$T_i \;=\; \int_{\Gamma_i} \frac{ds}{c_o(\mathbf{x},t_o) \;+\; \delta c(\mathbf{x},t) \;+\; \mathbf{u}(\mathbf{x},t)\cdot\tau}\;. \tag{3.22}$$

Expanding the integrand and keeping only leading order terms

$$T_i \;=\; \int_{\Gamma_i} \frac{ds}{c_o(\mathbf{x},t_o)} \;-\; \int_{\Gamma_i} \frac{\delta c(\mathbf{x},t) \;+\; \mathbf{u}(\mathbf{x},t)\cdot\tau}{c_o(\mathbf{x},t_o)^2}\, ds\;. \tag{3.23}$$

We now assume that the perturbed ray path is the same as the unperturbed ray path Γ_{oi} (determined from the reference ocean $c_o(\mathbf{x},t_o)$). This condition will be satisfied if $c_o(\mathbf{x},t_o) >> \delta c(\mathbf{x},t)$, which is the same criterion for the validity of the linearization. Then

$$\begin{aligned} T_i \;&=\; \int_{\Gamma_{oi}} \frac{ds}{c_o(\mathbf{x},t_o)} \;-\; \int_{\Gamma_{oi}} \frac{\delta c(\mathbf{x},t) \;+\; \mathbf{u}(\mathbf{x},t)\cdot\tau}{c_o(\mathbf{x},t_o)}\, ds \\ &=\; T_{\Gamma_{oi}} \;+\; \delta T_i\;. \end{aligned} \tag{3.24}$$

The perturbation travel time is

$$\delta T_i \;=\; -\int_{\Gamma_{oi}} \frac{\delta c(\mathbf{x},t) \;+\; \mathbf{u}(\mathbf{x},t)\cdot\tau}{c_o(\mathbf{x},t_o)}\, ds \tag{3.25}$$

and for the reciprocal transmission

$$\delta T_i^r \;=\; -\int_{\Gamma oi} \frac{\delta c(\mathbf{x},t) \;-\; \mathbf{u}(\mathbf{x},t)\cdot\tau}{c_o(\mathbf{x},t_o)}\, ds\ . \tag{3.26}$$

Note the negative sign associated with the current in the numerator of the integrand of (3.26). This arises in the reciprocal transmission since the unit tangent vector is now directed in the opposite $(-x)$ direction. Forming sums and differences of the reciprocal transmissions, and keeping only the leading order term, we arrive at

$$\delta T_i^+ \;=\; \frac{\delta T_i \;+\; \delta T_i^r}{2} \;=\; -\int_{\Gamma_{oi}} \frac{\delta c(\mathbf{x},t)}{c_o(\mathbf{x},t_o)^2}\, ds\ , \tag{3.27}$$

$$\delta T_i^- \;=\; \frac{\delta T_i \;-\; \delta T_i^r}{2} \;=\; -\int_{\Gamma_{oi}} \frac{\mathbf{u}(\mathbf{x},t)\cdot\tau}{c_o(\mathbf{x},t_o)^2}\, ds\ , \tag{3.28}$$

The problem has now separated. The sum of the reciprocal travel time perturbations is linearly related to the sound speed perturbation δc, while the difference is linearly related to the current $\mathbf{u}\cdot\tau$ along the ray path. Sound speed is directly proportional to temperature (θ), with an empirical relationship given by (Munk and Wunsch, 1979)

$$\frac{\delta c}{c_o} \;=\; \alpha\delta\theta\ , \tag{3.29}$$

where $\alpha \;=\; 3.2\times 10^{-3}$. Thus, Equation (3.27) can be considered a linear relationship between the sum of reciprocal travel time perturbations and perturbations in

temperature. Equations (3.27) and (3.28) constitute the acoustic forward problem for temperature and current velocity, respectively.

With a triangular array of transceivers, relative vorticity may also be determined. The formulation for vorticity follows in the footsteps of Rossby (1975). We must make the assumption that the fluid is steady during the time span of reciprocal transmissions. Then the line integral of fluid velocity between two points is directly proportional to the difference in travel time of two signals transmitted in the opposite direction. This relation follows from (3.28) and is expressed as

$$\delta T_i^- \;=\; -\,\frac{\overline{\mathbf{u}}}{c_o^2}\,R_i \tag{3.30}$$

where $\overline{\mathbf{u}}$ is the path averaged current and R_i is the ray path length. The line integral of the current between points R_1 and R_2 can be written as

$$\int_{R_1}^{R_2} \overline{\mathbf{u}} \cdot d\tau \;=\; \overline{\mathbf{u}}_{12}\,R_{12} \;=\; -c_o^2\,\delta T_{12}^- \,. \tag{3.31}$$

The line integral of the current around a triangle is then

$$\oint \overline{\mathbf{u}} \cdot d\tau \;=\; \sum_{i=1}^{3} \overline{\mathbf{u}}_{i,i+1}\,R_{i,i+1} \;=\; -\sum_{i=1}^{3} c_{oi,i+1}^2\,\delta T_{i,i+1}^- \,, \tag{3.32}$$

where the summation is cyclic. Invoking Stokes' theorem we obtain

$$\oint \overline{\mathbf{u}} \cdot d\tau \;=\; \int\int \mathbf{n} \cdot (\nabla \times \overline{\mathbf{u}})\,dxdy \;=\; A\,\overline{\zeta}\,, \tag{3.33}$$

where $\mathbf{n}$ is a unit normal in the vertical direction, A is the planar surface area, and $\overline{\zeta}$ is the average vorticity. This result tells us that the circulation is equivalent to the

areal averaged vorticity times the area. We can write the areal averaged vorticity as

$$\overline{\zeta} \;=\; -\frac{1}{A}\sum_{i=1}^{3} c_{oi,i+1}^{2}\;\delta T_{i,i+1}^{-}\;. \tag{3.34}$$

This equation constitutes the acoustic forward problem for vorticity.

Chapter 4

The Inverse Problem

4.1 Formulation of the Inverse Problem

The inverse problem in acoustic tomography can be thought of in the following manner: given measurements of arrival times of acoustic rays, and assuming a forward model of acoustic propagation, estimate the interior structure of the sampled medium. It should be noted that we are by no means limited solely to observations of acoustic arrival times (amplitudes could also be used), nor are we restricted to a ray theoretical forward model (normal modes or the parabolic equation method could just as easily be substituted). Travel time data and ray theory were used in this analysis due to the simplicity with which the inverse problem could be posed. Our ultimate goal is to obtain the best possible estimate of the model parameters, which in this case corresponds to an estimate of the structure (temperature, current velocity, vorticity) of the sampled ocean.

An understanding of the inverse problem requires a full understanding of the forward problem. We write the forward problem symbolically as a linearized relationship

$$\mathbf{Gm} = \mathbf{d} , \tag{4.1}$$

where $\mathbf{d}$ is a vector of observations , $\mathbf{m}$ is a vector of unknown parameters, and $\mathbf{G}$ is a coefficient matrix (data kernel) which represents the model. The acoustic forward problem can easily be placed in this form. Rewriting (3.27), we have

$$[\ \frac{-R_{ij}}{c_{oj}^2}\ ]\ \delta c_j\ =\ \delta T_i\ , \tag{4.2}$$

where the i index refers to a particular eigenray, the j index refers to a particular layer, and R_{ij} is the path length of ray i in layer j. A graphical representation of the data kernel (neglecting the $\frac{1}{c_{oj}^2}$ scale factor) is shown in Figure 4.1. The oceanic medium is divided into five layers and the ray spatial coverage corresponds to the identified eigenrays for the S1R2 or S2R1 case. Comparing (4.2) with (4.1), we see that for the acoustic tomographic case, the operator matrix $\mathbf{G}$ is given by $\frac{-R_{ij}}{c_{oj}^2}$, the model parameter vector $\mathbf{m}$ consists of sound speed perturbations δc_j, and the data vector $\mathbf{d}$ consists of acoustic travel times δT_i. The inverse of (4.1) can then be written symbolically as

$$\hat{\mathbf{m}}\ =\ \mathbf{G}^{-1}\mathbf{d}\ , \tag{4.3}$$

where $\hat{\mathbf{m}}$ is the best estimate of the model parameters $\mathbf{m}$ and $\mathbf{G}^{-1}$ is the inverse of $\mathbf{G}$.

Before constucting the inverse operator, we look at the relationship between the observations and the model parameters. The number of model parameters is not always (as a matter of fact, hardly ever) equal to the number of measurements one has available. This inequality has important consequences. Inverse problems can be separated into three classes: overdetermined problems (more data than unknowns), even determined problems (same number of equations as unknowns), and under-

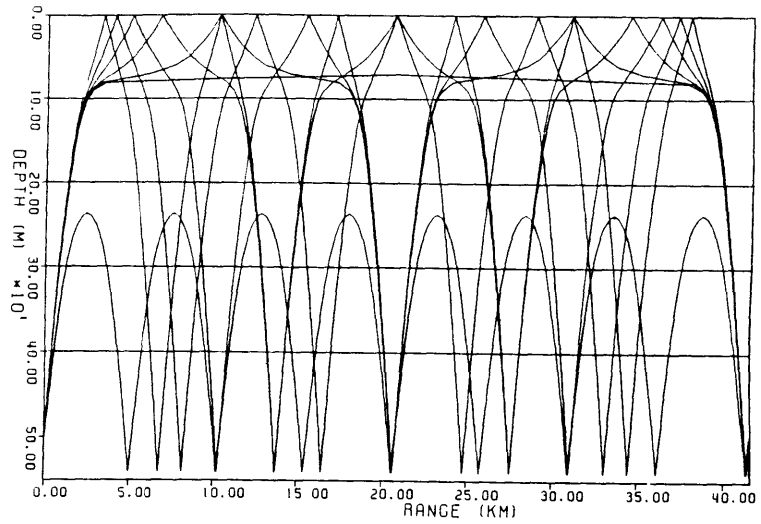

Figure 4.1. Eigenrays used for the S1R2 (and S2R1) inversion, divided into layers.

determined problems (more unknowns than data). Menke (1984) gives a simple and complete discussion of the inverse solutions to all three cases.

The overdetermined problem is equivalent to the conventional least squares approach, and the least squares solution to (4.1) is given by

$$\hat{\mathbf{m}} = [\mathbf{G}^T\mathbf{G}]^{-1}\mathbf{G}^T\mathbf{d} , \tag{4.4}$$

where $\mathbf{G}^T$ is the transpose of the data kernel $\mathbf{G}$. This estimate is not exact, but has an associated error of $\mathbf{e}^T\mathbf{e}$, where $\mathbf{e} = \mathbf{d}^{obs} - \mathbf{G}\hat{\mathbf{m}}$. The least squares solution gives the 'best' estimate in the sense that the Euclidean distance from the observations (L^2 norm) is minimized. It should be mentioned that the L^2 norm is not the only criterion for defining the error, but it is usually as reasonable as any other. The even determined case has the same number of model parameters as observations, and as such has only one solution with no estimation error (assuming the equations are linearly independent).

The underdetermined problem is deficient in that there are not enough observations to uniquely determine all of the model parameters. In this case, the matrix $\mathbf{G}^T\mathbf{G}$ is singular, and no unique inverse exists. The inverse solution to (4.1) is instead given by

$$\hat{\mathbf{m}} = \mathbf{G}^T[\mathbf{G}\mathbf{G}^T]^{-1}\mathbf{d} \; . \tag{4.5}$$

More than one solution with zero estimation error can be found for the underdetermined problem. To single out a particular solution, we are forced to apply an additional constraint. The constraint we impose is that the inverse solution is minimized (i.e., $\hat{\mathbf{m}}^T\hat{\mathbf{m}}$ is as small as possible). Again we note that this is not the only constraint which could be used, but it is a useful one.

A problem which is formally overdetermined may actually be underdetermined. This will be the case if the number of equations is greater than the number of observations, but the number of independent equations is less than the number of observations. A simple example of this will be provided in the context of tomography. Consider the gridded area of ray path coverage shown in Figure 4.2. Some blocks (such as block 3) have several rays passing through them, and hence are overdetermined. Other blocks (such as block 4) have no rays sampling them and are therefore underdetermined. Still others (such as blocks 1 and 2) contain rays, but they are sampled by equal arc lengths, thereby rendering the individual boxes underdetermined. In a problem of this nature we need to sort the unknown model parameters into two sets - overdetermined and underdetermined parameters. The overdetermined model parameters can be solved in a least squares sense and the underdetermined model parameters can be solved in a minimum solution length sense. This leads us to a reparameterization of the operator matrix via the singular value decomposition.

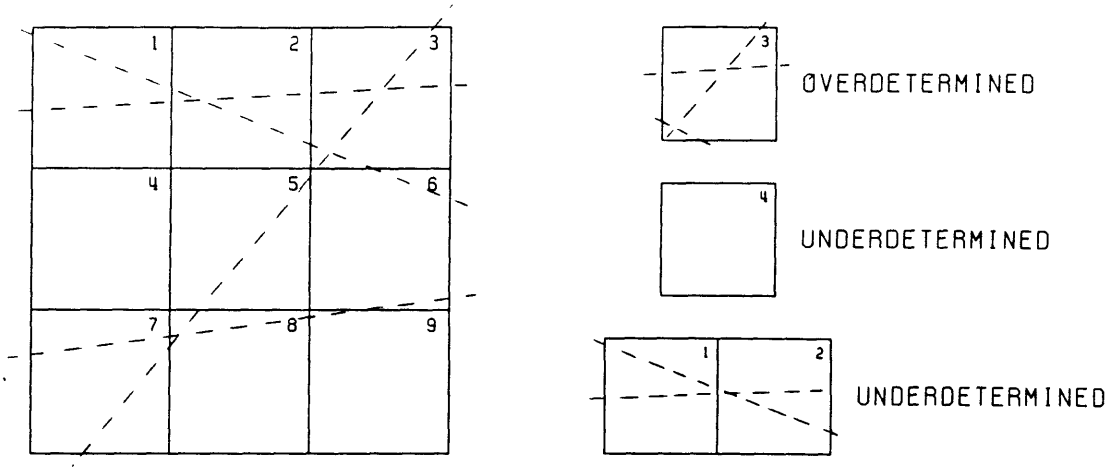

Figure 4.2. A tomographic coverage cartoon demonstrating the overdetermined and underdetermined nature of a simple problem.

4.2 The Singular Value Decomposition

The singular value (or spectral) decomposition is a factorization of the operator matrix into a set of orthonormal eigenvectors and associated eigenvalues. More specifically, the observations are decomposed into linear combinations of orthogonal eigenvectors, which in turn determine a linear combination of the model parameters. The value of this reparameterization is the ease with which it lends itself to the quantitative ranking of information content of the system. Thorough discussions of the singular value decomposition can be found in Lanczos (1961), Wiggins (1972), Jackson (1972), Wiggins et al., (1976), and Wunsch (1978).

Consider a system matrix $\mathbf{G}$ consisting of m rows and n columns. The singular value decomposition of $\mathbf{G}$ can be written (see Lanczos, 1961) as

$$\underset{m \times n}{\mathbf{G}} = \underset{m \times m}{\mathbf{U}} \quad \underset{m \times n}{\mathbf{\Lambda}} \quad \underset{n \times n}{\mathbf{V}^T} , \tag{4.6}$$

where

$$\mathbf{G}\mathbf{G}^T\mathbf{U} = \mathbf{U}\mathbf{\Lambda}^2 \ , \ \mathbf{G}^T\mathbf{G}\mathbf{V} = \mathbf{V}\mathbf{\Lambda}^2 \ . \tag{4.7}$$

The matrix $\mathbf{U}$ contains m orthonormal eigenvectors $\mathbf{u}_i$ which are the spectral components of the observation space. The eigenvectors $\mathbf{u}_i$ are associated with the columns (observations) of $\mathbf{G}$. Similarly, the matrix $\mathbf{V}$ contains n orthonormal eigenvectors $\mathbf{v}_i$ which are the spectral components of the model parameter space. The eigenvectors $\mathbf{v}_i$ are associated with the rows (model parameters) of $\mathbf{G}$. The matrix $\mathbf{\Lambda}$ is an $m \times n$ diagonal matrix which contains the singular values λ_i (with $\lambda_{i+1} \leq \lambda_i$). The size of the singular values determines the amplitude of the corresponding spectral components $\mathbf{u}_i$ and $\mathbf{v}_i$. The eigenvectors are orthogonal, so

$$\begin{aligned} \mathbf{U}\mathbf{U}^T &= \mathbf{U}^T\mathbf{U} = \mathbf{I}_m \\ \mathbf{V}\mathbf{V}^T &= \mathbf{V}^T\mathbf{V} = \mathbf{I}_n \ , \end{aligned} \tag{4.8}$$

where $\mathbf{I}_m$ is the $m \times m$ identity matrix and $\mathbf{I}_n$ is the $n \times n$ identity matrix.

We now take a closer look at the decomposed constituents of $\mathbf{G}$, paying particular attention to the dimensionality of the matrices. The $\mathbf{u}_i$ eigenvectors lie in an m-dimensional space and the $\mathbf{v}_i$ eigenvectors lie in an n-dimensional space. The linear system may be rank deficient (less independent equations than total equations). We consider a system of rank k, where $k \leq n$ or $k \leq m$. The eigenvalue

matrix Λ then contains k nonzero singular values. The singular value decomposition of $\mathbf{G}$ becomes

$$\underset{m \times n}{\mathbf{G}} = \underset{m \times k}{\mathbf{U}} \quad \underset{k \times k}{\Lambda} \quad \underset{k \times n}{\mathbf{V}^T}, \tag{4.9}$$

with the $\mathbf{U}_k$ and $\mathbf{V}_k$ matrices consisting of only the first k columns of $\mathbf{U}$ and $\mathbf{V}$, respectively. The other portions of the eigenvector matrices ($\mathbf{U}_{k+1,\ldots,m}$, $\mathbf{V}_{k+1,\ldots,n}$) are annihalated by the zeros corresponding to λ_i, $i > k$. The data and model parameter spaces spanning the null eigenvectors are referred to as the $\mathbf{U}_o$ and $\mathbf{V}_o$ null spaces. The operator matrix $\mathbf{G}$ contains no information concerning the null spaces.

The solution space consists of the space spanned by $\mathbf{V}_k$ and $\mathbf{U}_k$ (i.e., the parts of the eigenvector matrices which are not annihalated by zero eigenvalues). The solution data space is spanned by $\mathbf{U}_k$ and the solution model parameter space is spanned by $\mathbf{V}_k$. The remaining null eigenvectors ($\mathbf{U}_o$ and $\mathbf{V}_o$) span the null spaces. Since the solution and null eigenvectors are orthonormal by construction,

$$\mathbf{U}_k^T \mathbf{U}_k = \mathbf{V}_k^T \mathbf{V}_k = \mathbf{I}_k . \tag{4.10}$$

However, for $k < m, n$, the solution space does not span the complete data space or model space, so

$$\begin{aligned} \mathbf{U}_k \mathbf{U}_k^T &\neq \mathbf{I}_m \\ \mathbf{V}_k \mathbf{V}_k^T &\neq \mathbf{I}_n . \end{aligned} \tag{4.11}$$

These two relations express the resolvability of the data and model spaces, respectively, and will be considered in greater detail in the next section.

Before proceeding to the inverse solution, we give a simple geometrical interpretation of the decomposed eigenvectors (see Wiggins, 1972). The eigenvector $\mathbf{v}_1$, which corresponds to the largest singular value λ_1, is the vector most parallel to the rows of $\mathbf{G}$. Similarly, $\mathbf{u}_1$ is the vector most parallel to the columns of $\mathbf{G}$. The vectors $\mathbf{v}_2$ (orthogonal to $\mathbf{v}_1$) and $\mathbf{u}_2$ (orthogonal to $\mathbf{u}_1$) are then the vectors most parallel to the corresponding residuals. Continuing in this fashion it is seen that the residual is reduced as the eigenvectors corresponding to smaller and smaller eigenvalues are added. We will consider the consequences of this when we discuss the system variance in the next section.

We are now able to solve the inverse problem. By analogy to the least squares case, the solution is given as

$$\hat{\mathbf{m}} = \mathbf{V}_k \mathbf{\Lambda}_k^{-1} \mathbf{U}_k^T \mathbf{d} \; . \tag{4.12}$$

This expression can be obtained by substituting (4.6) into (4.4), and using the orthogonality conditions of (4.10). This particular least squares solution also satisfies the constraint that it minimizes the sum of the squares of the solution parameters (i.e., $\hat{\mathbf{m}}^T \hat{\mathbf{m}}$ is as small as possible). It can be shown that this solution has an estimation error $\mathbf{e}$ ($\mathbf{e} = \mathbf{d}^{obs} - \mathbf{G}\hat{\mathbf{m}}$) with no component in the solution data space and a parameter estimation $\hat{\mathbf{m}}$ with no component in the null model space (see Menke, 1984). In other words, solution (4.12) minimizes the arbitrary contributions of the null vectors.

We now look at the inverse estimate for the model parameters in greater detail. Rewriting (4.12) as a sum of eigenvectors $\mathbf{v}_i$, we have

$$\hat{\mathbf{m}} = \sum_{i=1}^{k} \frac{\mathbf{u}_i \cdot \mathbf{d}}{\lambda_i} \mathbf{v}_i \; . \tag{4.13}$$

For the acoustic tomography problem, we have

$$\delta c = \sum_{i=1}^{k} \frac{\mathbf{u}_i \cdot \delta T}{\lambda_i} \mathbf{v}_i \, . \tag{4.14}$$

The inverse solution for the model parameters (e.g. sound speed perturbations) is simply a linear combination of the observations (travel time deviations). The coefficient of each parameter eigenvector $\mathbf{v}_i$ is the amplitude of the ith spectral component contained in the observations (see Wiggins et al., 1976 for the linear filter analogue). The quantity is then scaled by $\frac{1}{\lambda_i}$, the inverse of the 'system response'.

The singular values of the observation and model parameter spaces for the S1R2 (or S2R1) case are shown in Figure 4.3, along with a plot of the associated singular vectors. This example has five singular values which correspond to sound speed perturbations in each of five layers in the vertical. Several features are worth mentioning. The singular vectors shown in Figures 4.3b,c correspond to the columns of the **U** and **V** matrices, respectively. A general trend in the structure of the eigenvectors is obvious. As the singular values λ_i decrease in size, the structure of the corresponding $\mathbf{u}_i$ and $\mathbf{v}_i$ eigenvectors becomes more complex and wavelike in nature. The singular vectors $\mathbf{u}_1$ and $\mathbf{v}_1$, corresponding to the largest singular value λ_1, indicate that the large scale (or low wavenumber) features of the problem are best determined. As singular vectors corresponding to smaller and smaller singular values are incorporated, smaller scale features (higher frequency components) surface in the inverse estimates. But the smaller scale features are not as well determined as the large scale features. This is evident as the small scale features are found in the eigenvectors which are scaled by small singular values (and thus have a small system response).

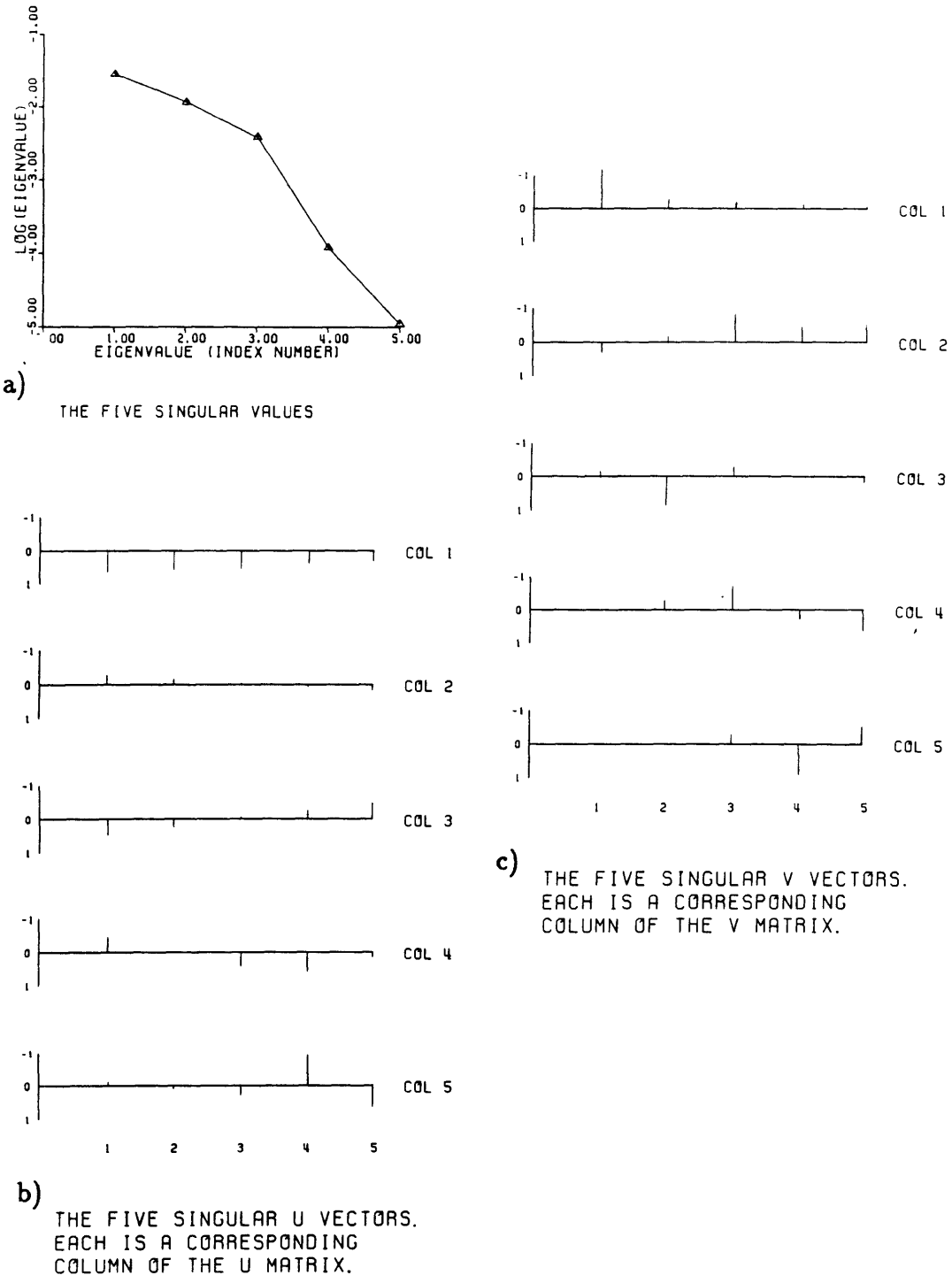

Figure 4.3. The singular values and singular vectors of the observation and model parameter spaces for the S1R2 (or S2R1) case.

Up to this point we have looked specifically at a noise-free system. We now consider the case of noisy measurements (i.e., uncertainty in the travel time measurements). Uncertainties in the observations lead to corresponding uncertainties in the model parameters. The forward problem may be written symbolically as

$$\mathbf{Gm} + \mathbf{n} \;=\; \mathbf{d} \;, \tag{4.15}$$

where $\mathbf{n}$ is a vector of observational noise. The estimation of the model parameters in the presence of noise is now a stochastic problem, and as such can be solved in the context of optimal estimation theory. Herein, we assume that the noise is uncorrelated from one measurement to the next, and also that the noise has a mean square expectation error of σ^2. For correlated noise the covariance matrix is no longer diagonal, but may be diagonalized with a suitable transformation.

We choose the minimum variance biased estimator as the best inverse solution to the stochastic problem. Allowing some bias in the solution reduces the large variance associated with small singular values acting on noisy measurements. The minimum variance biased estimate of (4.15) is (see Liebelt, 1967)

$$\hat{\mathbf{m}} \;=\; \mathbf{G}(\mathbf{G}\mathbf{G}^T + \hat{\sigma}^2\mathbf{I})\mathbf{d} \;, \tag{4.16}$$

where $\hat{\sigma}^2$ is the ratio of the noise variance to the solution variance. In terms of the spectrally decomposed eigenvectors, the model parameter estimate becomes (see Wiggins, 1972)

$$\hat{\mathbf{m}} \;=\; \sum_{i=1}^{k} \frac{\lambda_i(\mathbf{u}_i \cdot \mathbf{d})}{\lambda_i^2 + \hat{\sigma}^2}\, \mathbf{v}_i \;. \tag{4.17}$$

For the acoustic tomography case, we have

$$\delta c = \sum_{i=1}^{k} \frac{\lambda_i(\mathbf{u}_i \cdot \delta T)}{\lambda_i^2 + \hat{\sigma}^2} \mathbf{v}_i \,. \tag{4.18}$$

Singular values below the noise level are damped by the variance parameter $\hat{\sigma}^2$. In other words, contributions from the poorly determined parts of the solution (associated with small λ_i) are diminished by the variance cutoff. An alternative method which accomplishes the same task is to simply truncate the sum (4.17) when the singular values become small. The truncation procedure was used in this analysis.

4.3 Resolution and Variance

An inverse solution is really not complete without a discussion of the resolution and variance of the system. The singular value decomposition provides a simple framework for determining how well the inverted model parameters fit the data and how close the model parameter estimates are to the true values. The singular value decomposition also explicitly illustrates the influence which small singular vectors (corresponding to small singular values) have on the variance of the solution.

We first consider model parameter resolution. The relationship between the estimated parameters and the true values are obtained by substituting (4.1) into (4.3), which gives

$$\hat{\mathbf{m}} = \mathbf{G}^{-1}\mathbf{d} = \mathbf{G}^{-1}[\mathbf{G}\mathbf{m}] = [\mathbf{G}^{-1}\mathbf{G}]\mathbf{m} = \mathbf{R}_m\mathbf{m} \,, \tag{4.19}$$

with $\mathbf{R}_m$ being the model parameter resolution matrix. From the singular value decomposition and the orthogonality condition (4.8), it follows that

$$\mathbf{R}_m = \mathbf{G}^{-1}\mathbf{G} = [\mathbf{V}_k\mathbf{\Lambda}_k^{-1}\mathbf{U}_k^T][\mathbf{U}_k\mathbf{\Lambda}_k\mathbf{V}_k^T] = \mathbf{V}_k\mathbf{V}_k^T . \tag{4.20}$$

Each model parameter will be uniquely determined only if $\mathbf{R}_m = \mathbf{I}$. In other words, $\mathbf{V}_k$ must span the complete space of model parameters (i.e., no zero singular values) in order for the model parameters to be perfectly resolved. If $\mathbf{R}_m \neq \mathbf{I}$, then the estimate of the model parameters is not perfectly resolved but instead is a weighted average of the true model parameters.

The diagonal elements of $\mathbf{V}\mathbf{V}^T$ give a clue as to how well the individual model parameters are resolved. A value of unity indicates a perfectly resolved parameter whereas a smaller value corresponds to inadequate resolution. Figure 4.4 displays the diagonal elements for the S1R2 (or S2R1) case for a system of rank $k = 2$, 3, 4, and 5, respectively. Remember that this case has seven data measurements and five model parameters associated with five layers in the vertical, thus leading to perfect resolution for the rank $k = 5$ system. Needless to say, the resolution deteriorates as the number of expansion vectors is decreased. Note that the surface layer model parameter is nearly uniquely determined even for a rank $k = 2$ system. The model parameters associated with the lower two layers are poorly resolved for all but the perfectly resolved case. Layers two and three are fairly well resolved for a rank $k =$ 3 and 4 system.

We next consider data resolution, or alternatively the information density of the observations. The fit of the model parameter estimate with the observed data

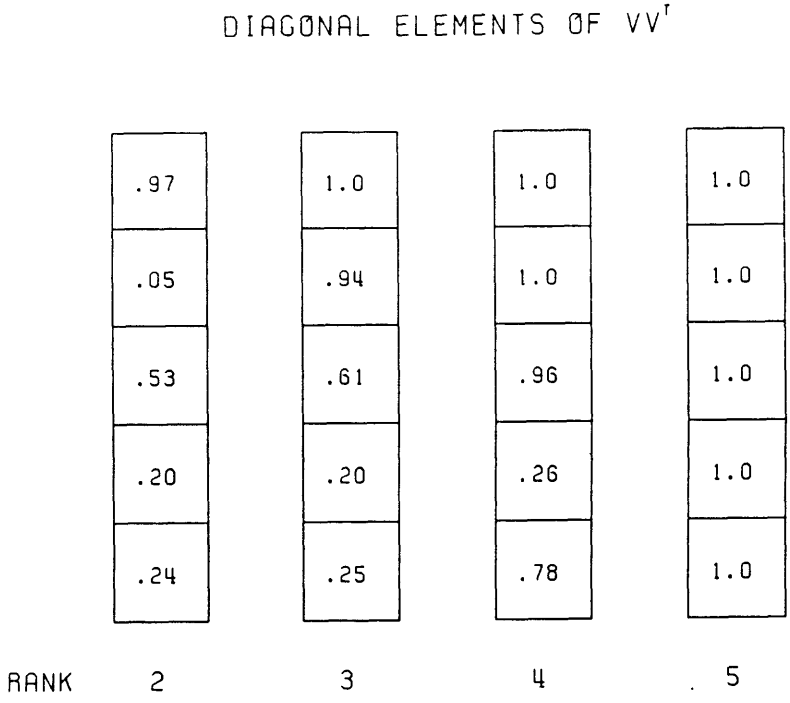

Figure 4.4. Model parameter resolution in each of five layers for a rank 2, 3, 4, and 5 S1R2 (or S2R1) system. The top box indicates resolution in the surface layer and the bottom box indicates resolution in the bottom layer.

is obtained by substituting (4.3) into (4.1), which gives

$$\mathbf{d}^{pre} = \mathbf{G}\hat{\mathbf{m}} = \mathbf{G}\,[\mathbf{G}^{-1}\mathbf{d}] = [\mathbf{G}\mathbf{G}^{-1}]\mathbf{d} = \mathbf{R}_d\mathbf{d}\,, \tag{4.21}$$

with *pre* meaning predicted and $\mathbf{R}_d$ being the data resolution matrix. From the singular value decomposition and the orthogonality condition (4.8), it follows that

$$\mathbf{R}_d = \mathbf{G}\mathbf{G}^{-1} = [\mathbf{U}_k\mathbf{\Lambda}_k\mathbf{V}_k^T][\mathbf{V}_k\mathbf{\Lambda}_k{}^{-1}\mathbf{U}_k^T] = \mathbf{U}_k\mathbf{U}_k^T\,. \tag{4.22}$$

The inverse solution has zero prediction error only if $\mathbf{R}_d = \mathbf{I}$. In other words, $\mathbf{U}_k$ must span the complete data space in order for the data to be perfectly resolved. If $\mathbf{R}_d \neq \mathbf{I}$, the solution has a nonzero prediction error. Alternatively, the data resolution matrix indicates which data are contributing independent information to the solution.

The diagonal elements of $\mathbf{U}\mathbf{U}^T$ for the S1R2 (or S2R1) case are shown in Figure 4.5 for a system of rank $k = 2$, 3, 4, and 5, respectively. A value of unity indicates a contribution of information which is completely independent of the other observations. Again note that the information resolution degrades as more expansion vectors are discarded. The most independent observation is the one located in the bottom box. This corresponds to the main RBR peak (see Figure 4.1). The other six boxes correspond to the six surface ducted arrivals. It is no surprise that these six boxes indicate poor information resolution as the associated eigenrays sample nearly the same surface region.

We now turn to the variance of the model parameter estimates. As we noted earlier, we chose to truncate the sum (4.17) for small singular value terms (as opposed to the tapered least squares approach), so we seek an estimate for the statisical error of (4.13). The variance of the jth parameter estimate is given by (see Wiggins, 1972)

$$E_j = \sigma^2 \sum_{l=1}^{k} \frac{\mathbf{v}_{jl}^2}{\lambda_l^2}, \tag{4.23}$$

where σ^2 is the variance of the observation. This expression clearly demonstrates the increase in the uncertainty of the model parameter estimate as the eigenvectors corresponding to the small singular values are added to the solution. This leaves us

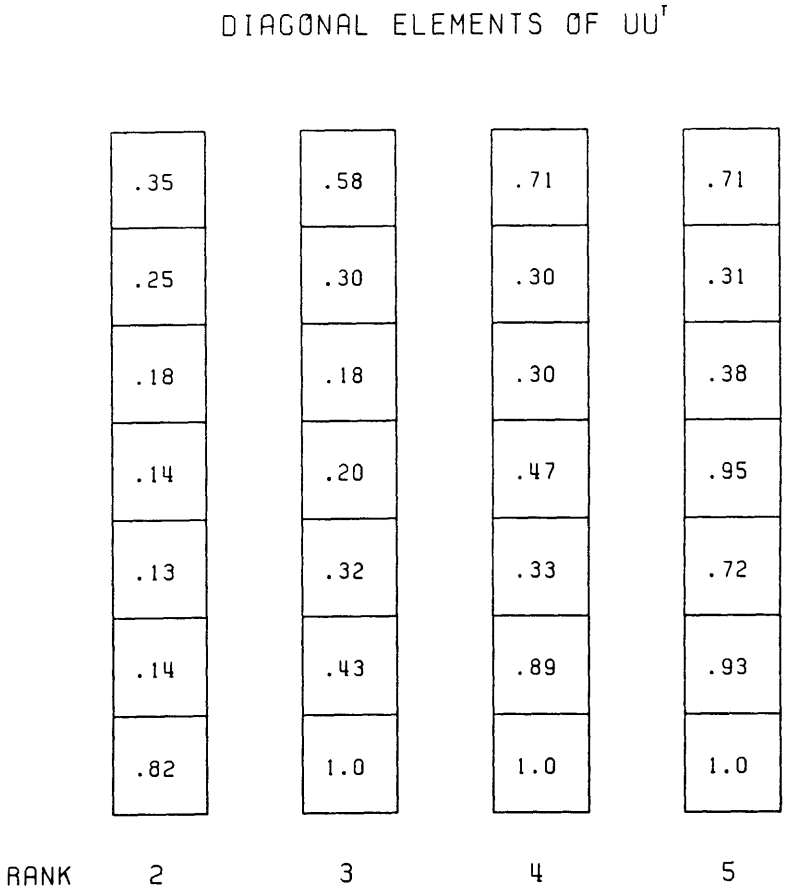

Figure 4.5. Data resolution (information density) for each of seven eigenrays for a rank 2, 3, 4, and 5 S1R2 (or S2R1) system. The top box corresponds to the 1SD eigenray, the second box to the 2SD eigenray, ..., and the bottom box corresponds to the main peak RBR eigenray.

with the conventional tradeoff between model resolution and variance. Resolution is enhanced by keeping the singular vectors associated with the small singular values, but at the same time the variance of the estimates blows up. Error bars for the inverse estimates will be shown with the plotted results in the next chapter.

Chapter 5

Oceanographic Variables

5.1 Temperature

Results of the October 1983 reciprocal tomography experiment in the Straits of Florida are now presented. Depth dependent inverse estimates of temperature along the three legs of the triangular array are presented first. Temperature time series for leg 1↔2, 1↔3, and 2↔3 are plotted in Figures 5.1a-c, respectively. Inverse estimates for a rank 1, 2, and 3 system are shown (i.e., the singular vectors corresponding to the largest, the two largest, and the three largest eigenvalues are kept). Rank 4 and 5 solutions (for the 1↔2 leg) and rank 4, 5, and 6 solutions (for the 1↔3 and 2↔3 legs) showed unrealistically large fluctuations in temperature due to the retention of small singular value terms. For comparison, STACS mooring temperature records, divided into vertical layers, are also plotted. Thermistor data from mooring 147 is used for comparison with temperature estimates for leg 1↔2 and thermistor data from mooring 148 is used for comparison with temperature estimates for legs 1↔3 and 2↔3. Note that the temperatures represent deviations from a reference day, chosen as October 19 (the first day of acoustic transmission). As previously mentioned, absolute temperatures are not available due to inaccuracies in the determination of the exact leg separation (and hence pulse arrival times).

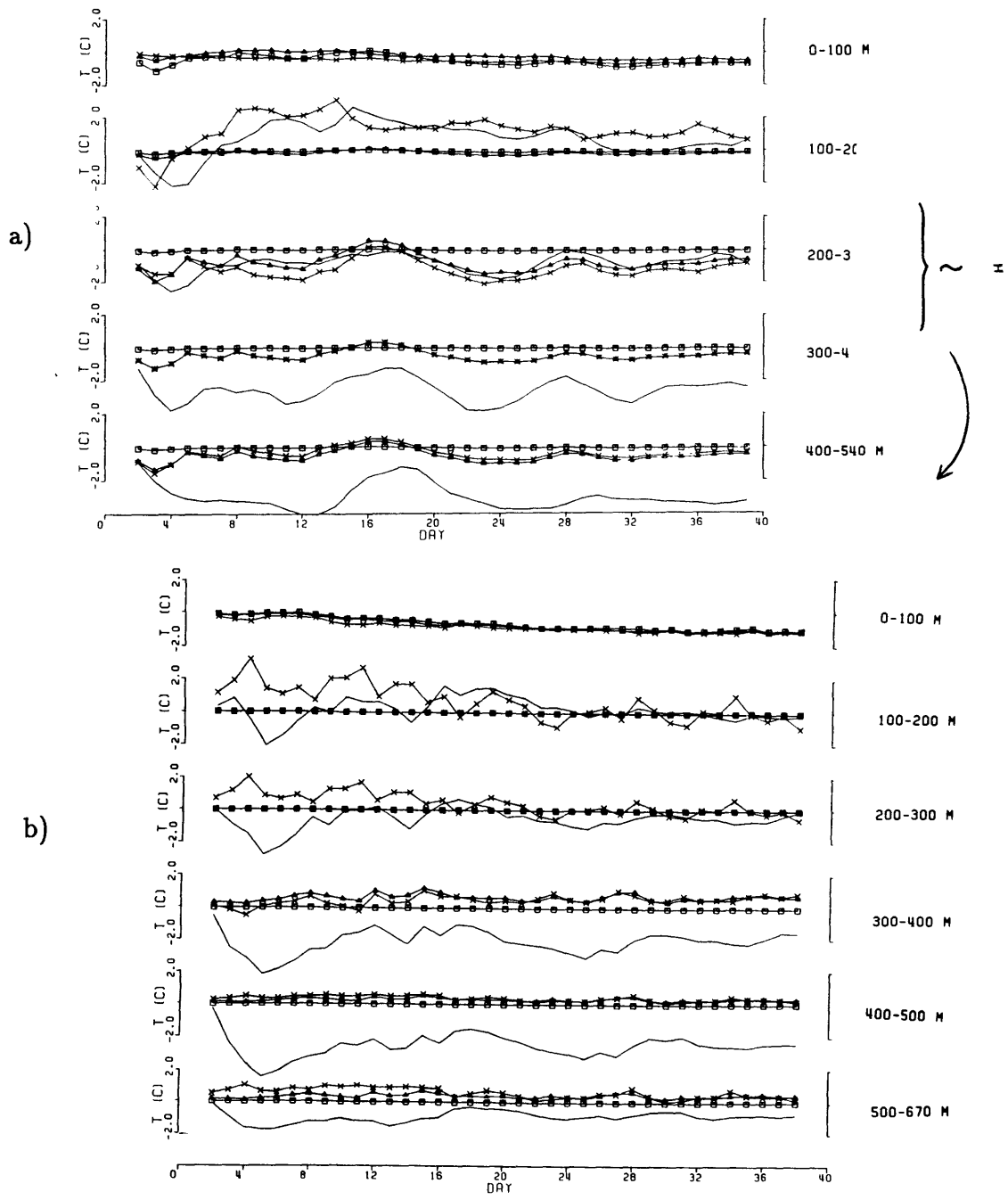

Figure 5.1. Inverse estimated temperature time series for (a)leg 1↔2 in comparison with directly measured temperatures at mooring 147, (b)leg 1↔3 in comparison with directly measured temperatures at mooring 148, and (c)leg 2↔3 in comparison with directly measured temperatures at mooring 148. Inverse estimates for a rank 1, 2, and 3 system are plotted for all three cases. Error bars for the rank 3 system are also included for each case.

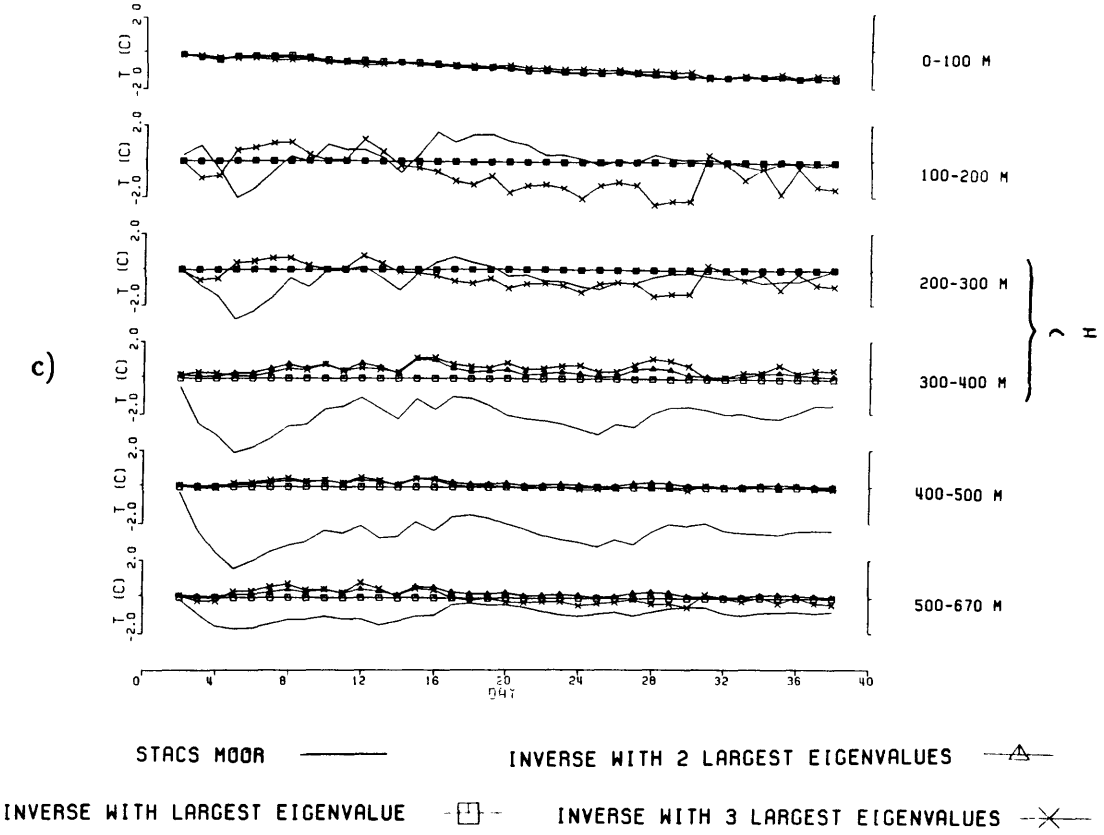

We now concentrate on leg 1↔2 (Figure 5.1a), which is aligned nearly directly with the core of the Florida Current. The inverse estimates for temperature are calculated using Equations (3.27) and (4.14). The sound speed perturbations are converted to temperature fluctuations with the empirical relation given in Equation 3.29. The error bars are for the rank 3 case and are computed from Equation (4.23), with $\sigma^2 = 1$ ms^2. The temperature estimate is the sum of two reciprocal transmissions, so the error is actually given by 2E. This is the expression used for the calculation of the errors given in Figures 5.1a-c. The rank 1 and 2 cases have smaller errors, but are less well resolved. The rank 3 system will be the focus of discussion as it appears to give the best resolution without sacrificing unreasonable variances.

The surface layer (0-100 m) shows a general cooling of approximately 0.5°C over the 40 day time series (mid October - end of November). There is no STACS mooring data in the surface layer for comparison. The next layer (100-200 m) shows an initial cooling of approximately 2°C over two days, then a rather rapid warming of about 4°C over the next five days. This large amplitude cooling/warming sequence is most likely indicative of a meandering of the Florida Current core over the 1↔2 leg, and matches quite well with the STACS mooring record. The remainder of the temperature record in the 100-200 m layer (days 10 - 40) indicates smaller scale fluctuations (1°- 2°C) and again corresponds quite well with the STACS mooring record. The middle layer shows temperature fluctuations of several degrees with a nearly ten day periodicity. This layer is in very close agreement with the STACS mooring record. The reason for this is that the main peak turning point is located in this layer (see Figure 4.1), and thus the layer is well sampled. The lowest two layers (300-400 m and 400-500 m) are poorly resolved (see Figure 4.4), but show similar trends in temperature variability (with a nearly ten day periodicity) with smaller amplitude fluctuations.

An offset in the mean value of the inverse estimated temperature, in comparison with the STACS mooring temperature record, is evident in the lowest two layers. The temperature offset, which appears as a bias in the inverse solution, can be rationalized in the following manner. First of all, the lowest two layers are inadequately resolved by acoustic ray paths. The inverse solution only contains information concerning the resolved part of the actual solution. Also, the small singular valued terms were cutoff from the solution as they introduced undesirably large variances in the well sampled layers. These small singular valued terms are responsible for much of the amplitude fluctuations in the deeper layers. By discarding these terms, the inverse solution tends to be as simple as possible, with a near zero mean and only small amplitude fluctuations about the mean.

Before looking at the other two legs of the array, we should make a few remarks concerning the comparison of the tomographic estimates with the moored current meter measurements. Temperatures observed at the current meters represents (in our case) a daily averaged measurement of the temperature field at a single point in space (the current meter). On the other hand, the tomographic estimates represent a spatially, as well as daily, averaged measure (over nearly 40 km) of the temperature field. In addition, the inverse procedure acts to smooth out highly energetic (small scale) fluctuations by weighting them with small singular values. Thus, we would expect the inverse estimation of temperature to show less small scale, high frequency variability in comparison with the current meter record. Low frequency fluctuations (with periodicities greater than several days) determined tomographically and with current meters should match up quite well.

We now turn to legs 1↔3 and 2↔3 (see Figures 5.1b,c). Temperature variability along these two legs is indicative of cross-stream temperature fluctuations in the eastern portion of the Florida Straits. Legs 1↔3 and 2↔3 are very poorly resolved in the vertical. Remember that we were only able to identify at most three eigenrays (and often times only two) from the processed acoustic data. The main peak, corresponding to propagation in the deeper layers, was always identifiable. The other peak (or sometimes two peaks) corresponded to a surface ducted path of propagation. This leaves us with three equations for six unknowns (temperature in each of six layers), and hence a highly underdetermined system. The temperature record for comparison is from mooring 148, which is displaced slightly east of the Florida Current core. We thus expect the moored current meter temperature time series to exhibit larger variability than the inverse estimate, which is spatially averaged over the more benign eastern region.

Inversion estimates for temperature along leg 1↔3 and 2↔3 will be discussed together as they show similar trends. The surface mixed layer (0-100 m) is rather

well sampled and indicates a cooling of about 0.5°C over the full time series. Temperature variability in the next two layers (100-200 m and 200-300 m) occurs at periodicities of several days to several weeks, with the amplitude of fluctuation being several degrees. Inverted temperature time series in these two layers compare favorably with the STACS mooring data over most of the record. Inversion estimates for the next three layers (300-400 m, 400-500 m and 500-670 m) indicate only small variability with respect to the reference day (October 19) in the deeper layers. This can be explained by the filtering nature of the inverse estimate and the inadequacy of resolution in these layers.

5.2 Current Velocity

Estimates for surface and near bottom current velocity along the three legs of the array are plotted in Figures 5.2a-c. The current estimates were obtained by inverting Equation (3.28). Several points concerning the estimation of current velocity should be made at this time. As previously mentioned, the final clock readings at the transceivers were not obtained. The clock errors are nonrecipropcal, and cancel in the calculation of temperature, but not in the calculation of current. Clock errors tend to drift nearly linearly with time, so a linear detrending of the three reciprocal transmissions was applied. The clock drifts cancel for transmission around a closed loop (the triangular array), so this constraint was adopted as a consistency check. A full layer inversion was not attempted due to lack of resolution, especially for the two cross-channel legs of the array. Instead, current estimates for the surface mixed layer (based on the surface ducted 1SD ray arrivals) and for the near bottom layer (based on the main peak RBR ray arrivals) are presented.

Before discussing the current velocities, a few remarks concerning the errors in the current estimate should be made. The current estimate is the difference of

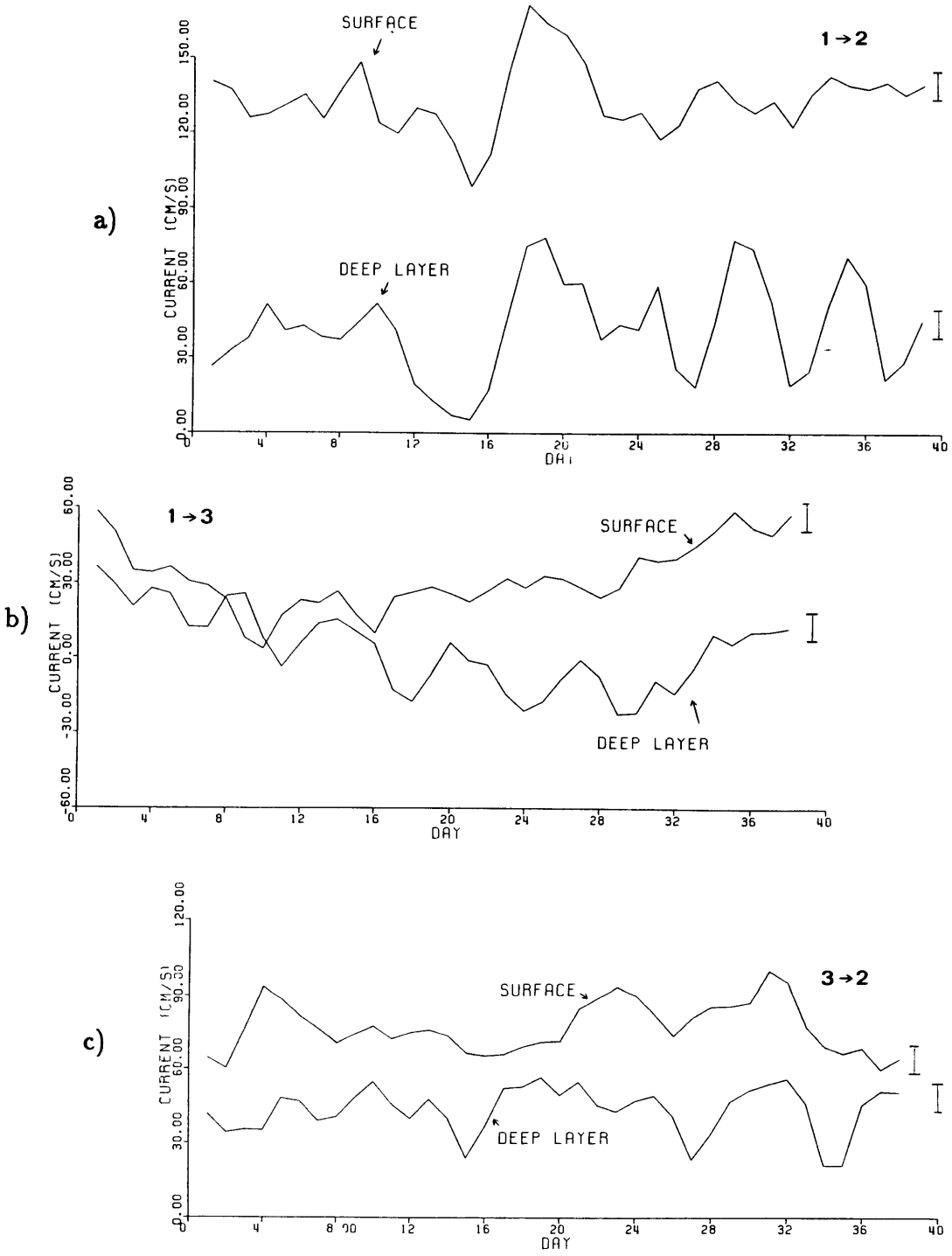

Figure 5.2. Estimated surface and near bottom current velocities, along with the estimated errors for the current estimate, for (a)leg 1→2, (b)leg 1→3, and (c)leg 3→2.

daily averages of reciprocal transmissions. Howe (1986) finds that the noise variance of the current (difference) estimate is about 10% that of the temperature (sum) estimate due to the elimination of the internal wave-induced noise by subtraction. Herein, we assume that an upper bound for the differential (current) noise variance is 25% of the summed (temperature) noise variance. Despite the smaller noise variance in comparison with the temperature estimate, the current estimate is much more sensitive to small errors. This is due to the weak signal of the current, which is typically several orders of magnitude smaller than the sound speed (temperature) perturbations.

Current velocity estimates for the north/south leg 1→2 of the array are shown in Figure 5.2a. The upper time series corresponds to surface velocities in the mixed layer and the lower time series is representative of current velocities at a depth of about 200 meters above the bottom. The surface currents are indicative of the Florida Current core and exhibit a mean speed of nearly 140 cm/s northward. The surface current fluctuates from a low of 100 cm/s to a high of 170 cm/s, with the larger fluctuations occuring at periods ranging from several days to nearly ten days. Surface mixed layer velocities are strongly influenced by changes in the local wind forcing, as well as meandering events.

Estimated velocities 200 meters above the bottom have a mean of about 50 cm/s with fluctuations of ±30 cm/s. The deeper velocities are remarkably coherent with the surface velocities and show the baroclinicity of the Florida Current, which reaches all the way to the bottom of the Florida Straits. From the two current estimates, a rough value for the vertical shear $\frac{\Delta v}{\Delta z}$ of the Florida Current is found to be $-5 \times 10^{-3} s^{-1}$. Returning to the near bottom layer, the large amplitude fluctuations at this depth are partly due to the main peak sampling of the deeper water. Remember that the main peak is composed of an envelope of rays with turning points from 50 meters above the bottom to 450 meters above the bottom.

On average the center of mass of the main peak is representative of propagation in a layer centered nearly 200 meters above the sea floor. Internal waves and multipath interference may shift this layer tens of meters upwards or downwards, and thus the acoustic signal will sample a somewhat different background velocity. Nevertheless, the low frequency trends are certainly indicative of near bottom flow variability.

We next look at flow along the two cross-channel legs of the array. Leg 1→3 is situated 65° from the axis of the Florida Current and leg 3→2 is nearly 60° from the axis. Currents along 1→3 are indicative of onshore flow (toward the Little Bahama Bank) and currents along 3→2 are indicative of offshore flow. Some of the prevailing northward flow through the Florida Straits is superimposed on the cross-stream structure as the legs are not directed normal to the Florida Current.

Surface velocities along leg 1→3 (Figure 5.2b) show a 30 cm/s average flow toward the Little Bahama Bank, with fluctuations of ±25 cm/s. The deeper velocities, representative of flow at a depth of about 250 meters above the bottom, suggest an onshore flow on average. Instances of a small offshore flow are also found, as is seen primarily during days 16-30. The offshore flow is most likely explained by the influx of westward flowing water passing through the Northwest Providence Channel. The signature of meandering events is not altogether obvious. This is probably due to the averaging of the current velocity over the 45 km range.

Surface velocities along leg 3→2 (Figure 5.2c) indicate a consistent offshore flow of nearly 80 cm/s. Fluctuations about the mean are on the order of 20 cm/s. Estimated current velocities at about 250 meters above the bottom also show a general offshore flow of 40±15 cm/s. Offshore currents along this leg are due to the projection of the northward flow of the Florida Current along 3→2, added to the inflow through the Northwest Providence Channel. Low frequency variability is again seen for a period band of several days to nearly two weeks.

5.3 Vorticity

The estimated vorticity for the area enclosed by the triangular array is plotted in Figure 5.3. Estimates for both the surface mixed layer (from the 1SD surface ducted ray arrivals) and a layer 200 meters above the bottom (from the main peak RBR ray arrivals) are given. The vorticity was obtained by inverting Equation (3.34). It should be mentioned that the vorticity is obtained directly from the acoustic travel time measurements, and does not pass through the filtering of the inverse procedure described in Chapter 4. The triangular tomographic array is situated in the eastern portion of the Florida Straits, and thus we expect a predominantly anticyclonic circulation. Remember that the estimated vorticity is an areal averaged measurement, and is calculated by the circulation around the array. The surface layer vorticity is representative of circulation in a horizontal plane in the mixed layer. On the other hand, the near bottom vorticity is representative of the circulation in a layer which is not horizontal but parallels the sloping bottom.

We first look at vorticity in the surface layer. The estimated vorticity is anticyclonic, with a mean of $-3 \times 10^{-5}\mathrm{s}^{-1}$ and fluctuations of $\pm 3 \times 10^{-5}\mathrm{s}^{-1}$. The vorticity signal is dominated by the northward flow of the Florida Current along leg 1→2. A strong anticyclonic circulation follows when the core of the Florida Current is directly in line with the north/south leg 1→2 of the array. Conversely, weaker anticyclonic circulation is the case when the core of the Florida Current migrates to the west of leg 1→2.

Interpretation of the estimated vorticity in a layer roughly 200 meters above the bottom is more complicated as we must now consider the sloping bottom. From Figure 5.3 we see that the deep layer vorticity has a near zero mean, with fluctuations of $\pm 8 \times 10^{-5}\mathrm{s}^{-1}$. Remember that the sampling of the deep layer is by an en-

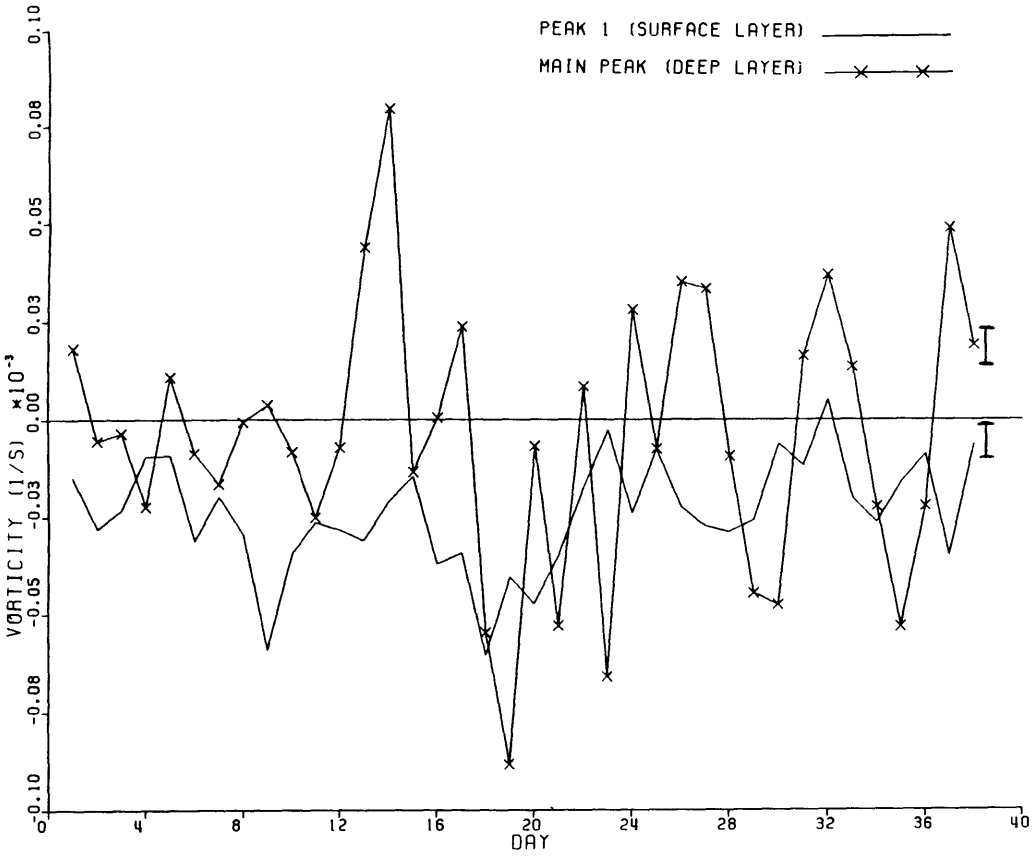

Figure 5.3. Estimated area-averaged vorticity, along with the estimated errors for the vorticity estimate, for the surface layer and the near bottom layer.

velope of rays with turning points spanning a wide range of depths. This may account for some of the high frequency oscillations in the estimations. The core of the deep Florida Current runs through the heart of the triangular array, filling the well between transceivers 1 and 2 and transceiver 3 (see Figure 2.2). Transceivers 1 and 2 are moored on a downward slope (facing east), whereas transceiver 3 is moored on an upward slope (facing east). Note that the current structure parallels the slope of the U-shaped seabed (see Figure 2.3). A lateral translation of the deep velocity structure eastward/westward can easily be seen to generate cyclonic/anticyclonic vorticity in the near bottom region.

We now take a closer look at the near bottom vorticity time series. Figure 5.4 compares the estimated vorticity with the horizontal downstream current shear ($\frac{\Delta v}{\Delta x}$) computed at a depth of 190 meters above the bottom using current velocity data from moorings 147 and 148. Approximating the relative vorticity ζ ($\zeta = \frac{\partial v}{\partial x} - \frac{\partial u}{\partial y}$) by $\frac{\Delta v}{\Delta x}$ is valid since $v >> u$ and $\frac{\partial}{\partial x} >> \frac{\partial}{\partial y}$. A phase lag of 18 hours was applied to the mooring 147 velocities to compensate for the 20 km displacement of mooring 148 to the north. As it turns out, the 18-hour phase lag did not alter the $\frac{\Delta v}{\Delta x}$ time series appreciably.

Figure 5.4. A comparison of the deep layer vorticity estimate with the horizontal downstream current shear between moorings 147 and 148 at a depth of nearly 190 meters above the bottom.

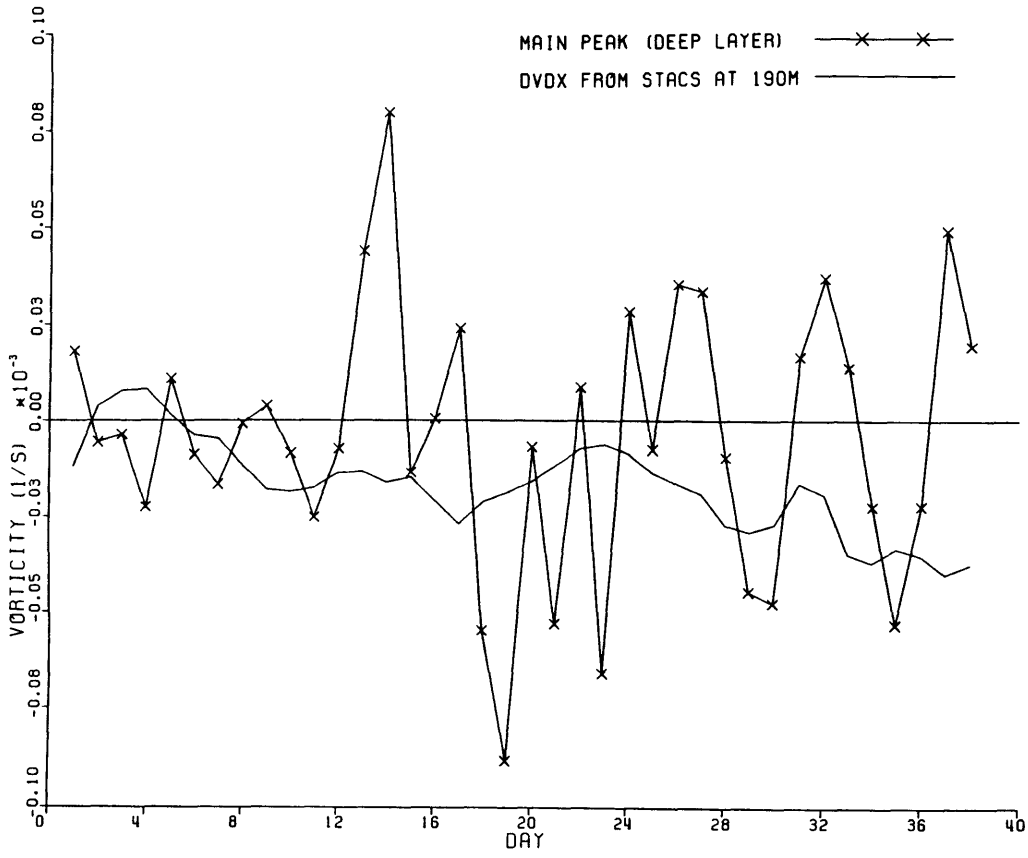

Note that the relative vorticity derived from the STACS mooring data is predominantly anticyclonic. Low frequency trends in the variability of the vorticity compare favorably with the tomographic estimate. The near bottom vorticity estimated tomographically encompasses a much larger area and is more representative of the vorticity on a larger scale in the eastern Florida Straits. Variability of the vorticity signal is again dominated by fluctuations of the deeper Florida Current core. When the upstream velocity along leg 1→2 drops off, the circulation becomes more cyclonic, and vice versa.

5.4 Discussion and Conclusions

A consistent oceanographic picture has evolved from the analysis of the acoustic data set generated during the October 1983 reciprocal tomography experiment in the Straits of Florida. Spatially averaged estimates of temperature, current velocity, and vorticity suggest large scale variability of the Florida Current in the eastern half of the Florida Straits at periods ranging from several days to nearly two weeks. Numerous previous authors have noted similar time scales of variability in this region using more conventional instrumentation. The physical oceanography of the eastern half of the Straits has been shown to be dominated by lateral shifting of the surface and subsurface core of the Florida Current. The cross-stream translation can be easily explained by a simple meandering of the Florida Current system. Also important in the region offshore of the Florida Current core is the large scale encroachment of water into the Straits through the Northwest Providence Channel.

The purpose of this thesis was to demonstrate the feasibility of acoustic tomography as a monitoring scheme for a shallow water environment, specifically the Florida Straits. I believe this goal has been met. The presence of a surface

mixed layer in the region proved fortuitous for this experiment. The mixed layer acts as a surface duct in trapping and propagating acoustic energy. This is the first instance in which surface ducted rays have been incorporated into a tomographic inversion. Coupled with the main peak refracted, bottom reflected ray arrivals, we are able to obtain depth dependent estimates of the oceanographic variables. Another promising result is the estimation of the large scale averaged vorticity in the eastern Florida Straits. Direct measurements of vorticity are always difficult to obtain (and even more difficult to interpret), especially from point measurements such as those obtained at current meters.

Tomography in a shallow water environment is a feasible measurement technique. The region of study in this experiment was highly range dependent in bottom bathymetry and contained an intense western boundary current passing through the array. The analysis provided in this treatise is simplistic in nature, utilizing linear inverse theory, two dimensional ray tracing, and no fancy signal processing for the peak identification of ray arrivals. More sophisticated techniques would certainly improve the results, but the results presented should be a very good first order approximation of the region of study. A complete understanding of the latest arriving main peak structure and of the multipath interference which gives rise to a distortion in the envelope of arrivals is probably the most difficult obstacle at this time. Identification and resolvability of the individual refracted, bottom reflected arrivals which comprise the main peak would allow much better resolution in the deeper layers. Analysis of this problem is a possible future endeavor. All in all, acoustic monitoring of oceanographic variability in a shallow water environment such as the Florida Straits provides a practical alternative to more conventional measurement systems.

REFERENCES

Brekhovskikh, L. and Y. Lysanov (1982) *Fundamentals of Ocean Acoustics.* Springer-Verlag, New York, 250 pp.

Brooks, D. A. (1975) Wind forced continental shelf waves in the Florida Current. Ph.D. Thesis, University of Miami, Florida, 268 pp.

Brooks, I. H., and P. P. Niiler (1977) Energetics of the Florida Current. *J. Mar. Res.*, **35**, 163–191.

Brown, M. G. (1984) Linearized travel time, intensity, and waveform inversions in the ocean sound channel-a comparison. *J. Acoust. Soc. Am.*, **75**, 1451–1461.

Cornuelle, B. (1983) Inverse methods and results from the 1981 ocean acoustic tomography experiment. Ph.D. Thesis, Massachusetts Institute of Technology/Woods Hole Oceanographic Institution, 359 pp.

Cornuelle, B., C. Wunsch, D. Behringer, T. Birdsall, M. Brown, R. Heinmiller, R. Knox, K. Metzger, W. Munk, J. Spiesberger, R. Spindel, D. Webb and P. Worcester (1985) Tomographic maps of the ocean mesoscale: pure acoustics. *J. Phys. Oceanogr.*, **15**, 133–152.

DeFerrari, H. A., and H. Nguyen (1986) Acoustic reciprocal transmission experiments, Florida Straits. *J. Acoust. Soc. Am.*, **79**, 299–315.

Düing, W. O., C. N. K. Mooers and T. N. Lee (1977) Low frequency variability in the Florida Current and some relations to atmospheric forcing from 1972 to 1974. *J. Mar. Res.*, **35**, 129–161.

Flatté, S. M., R. Dashen, W. Munk, K. Watson and F. Zachariasen (1979) *Sound Transmission through a Fluctuating Ocean.* Cambridge University Press, New York, 299 pp.

Hamilton K. G., W. L. Siegmann and M. J. Jacobson (1980) Simplified calculation of ray-phase perturbations to ocean-environmental variations. *J. Acoust. Soc. Am.*, **67**, 1193–1206.

Hela, I. (1952) The fluctuations of the Florida Current. *Bull. Mar. Sci. Gulf Carib.*, **4**, 241–248.

Howe, B. M. (1986) Ocean acoustic tomography: mesoscale velocity. Ph.D. Thesis, University of California, San Diego/Scripps Institution of Oceanography, 59 pp.

Howe, B. M., P. F. Worcester and R. C. Spindel (1987) Ocean acoustic tomography: mesoscale velocity. *J. Geophys. Res.*, **92**, 3785–3805.

Jackson D. D. (1972) Interpretation of inaccurate, insufficient, and inconsistent data. *Geophys. J. Roy. Ast. Soc.*, **28**, 97–109.

Johns, W. E. and F. Schott (1987) Meandering and transport variations of the Florida Current. *J. Phys. Oceanogr.*, **17**, 1128–1147.

Ko, D. S. (1987) Inversion methods and results from the 1983 Straits of Florida acoustic reciprocal transmission experiment. Ph.D. Thesis, University of Miami, Florida, 113 pp.

Ko, D. S., H. A. DeFerrari and P. Malonette-Rizzoli (1989) Temperature, current, and vorticity

Lanczos, C. (1961) *Linear Differential Operators.* Van Nostrand, London, 564 pp.

Leaman K. D. and R. L. Molinari (1987) Topographic modification of the Florida Current by Little Bahama and Great Bahama Banks. *J. Phys. Oceanogr.*, **17**, 1724–1736.

Leaman K. D., R. L. Molinari and P. S. Vertes (1987) Structure and variability of the Florida Current at 27 °N:April 1982-July 1984. *J. Phys. Oceanogr.*, **17**, 563–583.

Lee, T. N. and D. A. Mayer (1977) Low-frequency current variability and spin-off eddies along the shelf off southeast Florida. *J. Mar. Res.*, **35**, 193–219.

Lee, T. N., F. A. Schott and R. J. Zantopp (1985) Florida Current: low frequency variability as observed with moored current meters during April 1982 to June 1983. *Science*, **227**, 298–302.

Liebelt, P. B. (1967) *An Introduction to Optimal Estimation*, Addison-Wesley, Reading, Mass., 273 pp.

Malloy, R. J. and R. J. Hurley (1970) Geomorphology and geologic structure: Straits of Florida. *Geol. Soc. of Am. Bull.*, **81**, 1947-1972.

Medwin, H. (1984) Speed of sound in sea water: a simple equation for realistic parameters. *J. Acoust. Soc. Am.*, **58**, 1318–1319.

Menke W. (1984) *Geophysical Data Analysis: Discrete Inverse Theory.* Academic Press, Orlando, Florida, 260 pp.

Metzger Jr., K. (1983) Signal processing equipment and techniques for use in measuring ocean acoustic multipath structures. Cooley Electronics Laboratory Technical Report no. 231, University of Michigan, 268 pp.

Molinari, R. L., G. A. Maul, F. Chew, W. D. Wilson, M. Bushnell, D. Mayer, K. Leaman, F. Schott, T. N. Lee, R. Zantopp, J. Larsen and T. Sanford (1985a) Subtropical Atlantic Climate Studies: Introduction. *Science*, **227**, 292–295.

Molinari, R. L., W. D. Wilson and K. D. Leaman (1985b) Volume and heat transports of the Florida Current: April 1982 to August 1983. *Science*, **227**, 295–297.

Monjo C. L. (1987) Modeling of Acoustic Transmission in the Straits of Florida acoustic reciprocal transmission experiment. Ph.D. Thesis, University of Miami, Florida, 139 pp.

Montgomery, R. B. (1938) Fluctuations in monthly sea level on eastern U. S. coast as related to dynamics of western North Atlantic Ocean. *J. Mar. Res.*, **1**, 165–185.

Munk, W. and C. Wunsch (1979) Ocean acoustic tomography: a scheme for large scale monitoring. *Deep Sea Res.*, **26A**, 123–161.

Munk, W. and C. Wunsch (1982) Observing the oceans in the 1990s. *Phil. Trans. Roy. Soc. London*, **A307**, 439–464.

Ocean Acoustic Tomography Group, The (1982) A demonstration of ocean acoustic tomography. *Nature*, **299**, 121–125.

Officer, C. B. (1958) *Introduction to the Theory of Sound Transmission.* McGraw-Hill, New York, 284 pp.

Palmer, D. R., L. M. Lawson, D. A. Seem and Y. H. Daneshzadeh (1985) Ray path identification and acoustic tomography in the Straits of Florida. *J. Geophys. Res.*, **90**, 4977–4989.

Parr, A. E. (1937) Report on hydrographic observations at a series of anchor stations across the Straits of Florida. *Bull. Bingham Oceanogr. Coll.*, **6**, 1–62.

Pillsbury, J. E. (1891) The Gulf Stream-A description of the methods employed in the investigation, and the results of the research. *U. S. Coast Geodetic Survey Rep. for 1890*, app. **10**, 461–620.

Richardson, W. S. and W. J. Schmitz, Jr. (1965) A technique for the direct measurement of transport with application to the Straits of Florida. *J. Mar. Res.*, **23**, 172–185.

Richardson, W. S., W. J. Schmitz, Jr. and P. P. Niiler (1969) The velocity structure of the Florida Current from the Straits of Florida to Cape Fear. *Deep Sea Res.*, **16**(supp.), 225–231.

Rossby, T. (1975) An oceanic vorticity meter. *J. Mar. Res.*, **33**, 213-222.

Schmitz Jr., W. J. (1969) On the dynamics of the Florida Current. *J. Mar. Res.*, **27**, 121–150.

Schott, T.N., T. N. Lee, and R. Zantopp (1988) Variability of structure and transport of the Florida Current in the period range of days to seasonal. *J. Phys. Oceanogr.*, **18**, 1209–1230.

Spain, P. F., D. L. Dorson and T. Rossby (1981) Pegasus: a simple, acoustically tracked, velocity profiler. *Deep Sea Res.*, **28A**, 1553–1567.

Spindel, R. C. (1985) Signal processing in ocean tomography.

Steinberg, J. C. and T. G. Birdsall (1966) Underwater sound propagation in the Straits of Florida. *J. Acoust. Soc. Am.*, **39**, 301–315.

Steinberg, R. C., J. G. Clark, H. A. DeFerrari, M. Kronengold and K. Yacoub (1972) Fixed-system studies of underwater acoustic propagation. *J. Acoust. Soc. Am.*, **52**, 1521–1536.

Stoughton, R. B., S. M. Flatté and B. M. Howe (1986) Acoustic measurements of internal wave rms displacement and rms horizontal current off Bermuda in late 1983. *J. Geophys. Res.*, **91**, 7721–7732.

Tolstoy, I. and C. S. Clay (1966) *Ocean Acoustics: Theory and Experiment in Underwater Sound.* McGraw-Hill, New York, 293 pp.

Vertes, P. R. and K. L. Leaman (1984) The Subtropical Atlantic Climate Study: summary of RSMAS Pegasus observations in the Florida Straits. University of Miami RSMAS report no. 84002, 172 pp.

Wertheim G. K. (1954) Studies of the electric potential between Key West, Florida and Havana, Cuba. *Trans Am. Geophys. Un.*, **35**, 872–882.

Wiggins, R. A. (1972) The general linear inverse problem: implication of surface waves and free oscillations for earth structure. *Rev. Geophys. Space Phys.*, **10**, 251–285.

Wiggins, R. A., K. L. Larner and R. D. Wisecup (1976) Residual statics analysis as a general linear inverse problem. *Geophys.*, **41**, 922–938.

Wunsch, C., D. V. Hansen and B. D. Zetler (1969) Fluctuations of the Florida Current inferred from sea level records. *Deep Sea Res.*, **16**(supp.), 447–470.

Wunsch, C. and M. Wimbush (1977) Simultaneous pressure, velocity and temperature measurements in the Florida Straits. *J. Mar. Res.*, **35**, 75–104.

Wunsch, C. (1978) The North Atlantic General Circulation wets of 50 °W determined by inverse methods. *Rev. Geophys. Space Phys.*, **16**, 583–620.

Wüst, G. (1924) Florida und Antillenstrom, eine hydrodynamische untersuchung. Veröff. Inst. Meeresk, Univ. Berlin, NFA **12**, 48 pp.